Differentiation of benign and malignant breast tumors by *in-vivo* three-dimensional parallel-plate diffuse optical tomography

Regine Choe
Soren D. Konecky
Alper Corlu
University of Pennsylvania
Department of Physics & Astronomy
209 S. 33rd Street
Philadelphia, Pennsylvania 19104
E-mail: rgchoe@alumni.upenn.edu

Kijoon Lee
Nanyang Technological University
School of Chemical and Biomedical Engineering
Division of Bioengineering
Singapore 637457
    and
University of Pennsylvania
Department of Physics & Astronomy
209 S. 33rd Street
Philadelphia, Pennsylvania 19104

Turgut Durduran
University of Pennsylvania
Department of Physics & Astronomy
209 S. 33rd Street
Philadelphia, Pennsylvania 19104
    and
Hospital of the University of Pennsylvania
Department of Radiology
3400 Spruce Street
Philadelphia, Pennsylvania 19104

David R. Busch
Saurav Pathak
University of Pennsylvania
Department of Physics & Astronomy
209 S. 33rd Street
Philadelphia, Pennsylvania 19104

Brian J. Czerniecki
Julia Tchou
Douglas L. Fraker
Hospital of the University of Pennsylvania
Department of Surgery
3400 Spruce Street
Philadelphia, Pennsylvania 19104

Angela DeMichele
Hospital of the University of Pennsylvania
Department of Medicine (Hematology/Oncology)
3400 Spruce Street
Philadelphia, Pennsylvania 19104

Britton Chance
University of Pennsylvania
Department of Biochemistry & Biophysics
3700 Hamilton Walk
Philadelphia, Pennsylvania 19104

Simon R. Arridge
Martin Schweiger
University College London
Department of Computer Science
Gower Street
London, WC1E 6BT
United Kingdom

Joseph P. Culver
Washington University
School of Medicine
Department of Radiology
Mallinckrodt Institute of Radiology
St. Louis, Missouri 63110
    and
University of Pennsylvania
Department of Physics & Astronomy
209 S. 33rd Street
Philadelphia, Pennsylvania 19104

Mitchell D. Schnall
Hospital of the University of Pennsylvania
Department of Radiology
3400 Spruce Street
Philadelphia, Pennsylvania 19104

Mary E. Putt
University of Pennsylvania
Department of Biostatistics & Epidemiology
423 Guardian Drive
Philadelphia, Pennsylvania 19104

Mark A. Rosen
Hospital of the University of Pennsylvania
Department of Radiology
3400 Spruce Street
Philadelphia, Pennsylvania 19104

Arjun G. Yodh
University of Pennsylvania
Department of Physics & Astronomy
209 S. 33rd Street
Philadelphia, Pennsylvania 19104

Address all correspondence to Regine Choe, Department of Physics and Astronomy, University of Pennsylvania, 209 S. 33rd St., Philadelphia, PA, 19104; E-mail: rgchoe@alumni.upenn.edu

Abstract. We have developed a novel parallel-plate diffuse optical tomography (DOT) system for three-dimensional *in vivo* imaging of human breast tumor based on large optical data sets. Images of oxy-, deoxy-, and total hemoglobin concentration as well as blood oxygen saturation and tissue scattering were reconstructed. Tumor margins were derived using the optical data with guidance from radiology reports and magnetic resonance imaging. Tumor-to-normal ratios of these endogenous physiological parameters and an optical index were computed for 51 biopsy-proven lesions from 47 subjects. Malignant cancers ($N=41$) showed statistically significant higher total hemoglobin, oxy-hemoglobin concentration, and scattering compared to normal tissue. Furthermore, malignant lesions exhibited a twofold average increase in optical index. The influence of core biopsy on DOT results was also explored; the difference between the malignant group measured before core biopsy and the group measured more than 1 week after core biopsy was not significant. Benign tumors ($N=10$) did not exhibit statistical significance in the tumor-to-normal ratios of any parameter. Optical index and tumor-to-normal ratios of total hemoglobin, oxy-hemoglobin concentration, and scattering exhibited high area under the receiver operating characteristic curve values from 0.90 to 0.99, suggesting good discriminatory power. The data demonstrate that benign and malignant lesions can be distinguished by quantitative three-dimensional DOT. © *2009 Society of Photo-Optical Instrumentation Engineers.* [DOI: 10.1117/1.3103325]

1 Introduction

Breast cancer is one of the most common cancers among women. Approximately one in eight women in the United States will develop breast cancer during their lifetime, and, of these, about 20–30% will ultimately die of the disease.[1] Thus, early detection and accurate diagnosis of breast cancer are important. Existing clinical methods used for breast cancer screening and diagnosis, however, have drawbacks. X-ray mammography, for example, has an $\sim 22\%$ false-negative rate in women under 50[2] and sometimes cannot accurately distinguish between benign and malignant tumors.[3] Even though the false-positive rate of individual mammography is less than 10%,[4,5] 18% of women with no breast cancer will have undergone a biopsy after 10 mammograms.[5] Techniques such as ultrasound and magnetic resonance imaging (MRI) are sometimes used in addition to X-ray mammography, but they have limitations such as high cost, low throughput, limited specificity (MRI), and low sensitivity (ultrasound). Thus, new methods are needed to detect cancers earlier for treatment, to detect cancers missed by mammography,[6–8] to reduce the false-positive rate,[4,5] and to monitor tumor progression during cancer therapy.

Near-infrared (NIR) diffuse optical tomography (DOT) and spectroscopy (DOS) are tools that rely on functional processes for contrast and therefore have the potential to enhance sensitivity and specificity of breast cancer detection/diagnosis. DOT and DOS utilize nonionizing, low-power NIR light and are noninvasive and rapid. These diffuse optical methods measure wavelength-dependent tissue optical absorption coefficients, which in turn provide access to blood dynamics, total hemoglobin concentration (THC), tissue blood oxygen saturation (StO_2), and concentrations of water and lipid. Tissue properties accessible to DOT and DOS techniques have been demonstrably different in tumors compared to normal tissues.[9–26] The microscopic origin of tumor optical absorption contrast has been partially explored through the positive correlation of microvessel density and total hemoglobin concentration.[13,27,28] Similarly, mean size and volume fraction of the nucleus and nucleolus measured by microscopy have been correlated with light scattering measured by DOT.[29] The optical contrast in rapidly growing tumors is physiologically plausible, because these tissues often exhibit increased vascularity, altered oxygen content, and altered cellular structures at the microscopic scale.[30–35] Finally, DOT and DOS are attractive for applications such as cancer therapy that require frequent monitoring of physiological parameters. Thus far, changes in tumor contrast during therapy have exhibited agreement with physiological expectations[18,36] and with observations made by other imaging modalities.[19,27,37–39]

To date, optical data from sizable numbers of tumors (i.e., more than 30 tumors) have been reported by several research groups.[23–26,40,41] These results generally indicate that optical methods are capable of distinguishing lesions from healthy background tissue.[42] Demonstrations of a clear distinction between benign and malignant tumors, however, have been scarce, either due to a lack of benign lesion data[25,40] or to a limited three-dimensional (3-D) imaging capability.[23,24] Even the systems geared towards 3-D image reconstruction[26,41] have not as yet explored the full capability of diffuse optical tomography. Better characterization of malignant and benign lesions is anticipated through improvements in spatial resolution of instrumentation and reconstruction algorithms, and also through an increase in spectral information.[42] In order to improve the spatial resolution, for example, the number of source and detector positions covering the whole breast should be very large.[43] DOT also relies heavily on reconstruction algorithm quality for accurate quantification of optical properties; optimization of such algorithms is still an open arena for further development and is a key factor for improved image fidelity.

In this contribution, we report tumor contrast extracted from 3-D reconstructions of 51 breast tumors acquired using a parallel-plate DOT system. In addition to measurement geometry, our approach differs from others as a result of its very large data-set size with on- and off-axis measurements for full 3-D reconstruction and its highly optimized reconstruction schemes. The reconstruction algorithm employs iterative nonlinear methods for accuracy, multispectral data for reliable determination of chromophore concentrations and scattering parameters, parallel computing for speed, and spatially variant regularization for image artifact suppression. Furthermore, in order to avoid complications from image artifacts and lack of optical contrast in some lesions, in this study we have used information from dynamic contrast-enhanced MRI (DCE-MRI) to confirm and assign tumor margins. In total, these strategies improve the extraction of tumor-to-normal optical

contrast from 3-D oxy-hemoglobin, deoxy-hemoglobin, and scattering DOT images.

Briefly, malignant cancer showed statistically significant higher total hemoglobin concentration and scattering compared to normal tissue, with a twofold average increase in an optical index derived from intrinsic optical parameters. We did not observe statistically significant differences due to core biopsy in the malignant cancer group; potential bleeding due to core biopsy did not influence DOT results for those measured more than 1 week after core biopsy. Total hemoglobin concentration, blood oxygenation, and scattering were distinguishably lower in a cyst, whereas the difference between tumor and normal tissues for a fibroadenoma and a lobular carcinoma *in situ* were not apparent. Among many parameters, tumor-to-normal ratios of total hemoglobin concentration, scattering, oxy-hemoglobin concentration and the optical index demonstrated values of the AUC [area under the receiver operating characteristic (ROC) curve] higher than 0.9, suggesting good discriminatory power for resolving malignant from benign lesions.

The remainder of this paper is organized as follows. The Methods section provides demographic and histopathologic information about the subjects; it also describes the DOT instrument, the human subject measurement protocol, 3-D image reconstruction procedures, procedures for tumor-to-normal DOT parameters extraction, and statistical analysis. The Results section presents the data and demonstrates a correlation between DOT and DCE-MRI images using a representative case for each lesion type. This section also presents a comparison of tumor-to-normal DOT parameters among benign, malignant, and biopsied malignant groups. The Discussion section critiques our analysis method, compares results with other DOT/DOS studies, and gives suggestions for future improvements. In addition, supplementary material (Appendix) about measurement and analysis details are provided with the paper.

2 Methods

2.1 *DOT Instrumentation*

Our parallel-plate DOT system has been characterized using tissue phantoms simulating the breast with tumors.[44] The system consists of a light-source module, a table with a built-in Intralid/Ink fluid tank (i.e., the "breast box"), and a detection module. The light-source module is comprised of laser diodes, optical switches and optical fibers. Six NIR laser diodes are connected to a 6×1 optical switch, which in turn is connected to a 1×45 optical switch. The 45 optical fibers from this switch are arranged on a 9×5 grid pattern at the compression plate as seen in Fig. 1. Of the six lasers, four (690, 750, 786, and 830 nm) are sinusoidally intensity modulated at 70 MHz for frequency-domain measurements. Out of 47 patients, the first 15 patients were measured using this laser configuration (four wavelengths). Later, 11 patients were measured with an additional continuous-wave laser at 650 nm, and 23 patients were measured with continuous-wave lasers at 650 and 905 nm. These additional lasers were added to improve separation of chromophore contributions based on findings in Refs. 45 and 46.

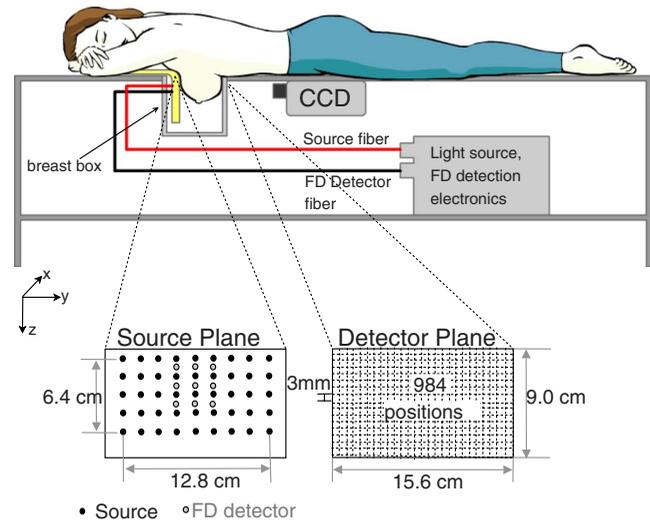Subjects lie in a prone position on the table with breasts positioned inside the breast box, which contains an Intralipid/

Fig. 1 Schematic of the parallel plate diffuse optical tomography instrument. A female subject lies in prone position on a bed with her breasts inside the breast box filled with an Intralipid/Ink fluid. Continuous-wave transmission andfrequency-domain remission measurements are performed simultaneously by a CCD camera and nine Avalanche Photodiodes connected by fibers on the source plate for 45 source positions at multiple wavelengths.

Ink fluid whose optical properties are similar to breast tissue ($\mu_a = 0.05$ cm^{-1} and $\mu_s' = 8$ cm^{-1} at 786 nm). The fluid is made with an Intralipid scattering agent and an India ink absorption agent. The breast box is made of black-pigment coated aluminum, with one side replaced by an antireflection coated plexiglass viewing window.

The compression plate also contains nine optical fibers in a 3×3 grid for frequency-domain detection. The detection has two measurement modes: a remission frequency-domain measurement mode and a transmission continuous-wave measurement mode. The frequency-domain measurements utilize homodyne techniques[47] to provide an initial estimate of breast bulk optical properties for image reconstruction. Transmission continuous-wave data at the viewing window are collected by a lens-coupled 16-bit charge-coupled-device (CCD) camera.

Our DOT instrumentation was designed to provide the large data sets essential for full 3-D reconstruction. The lens-coupled CCD in our system contains the largest number of on-axis and off-axis measurements covering the whole breast among 3-D DOT instruments.[13,14,16,17,20,21,48] For example, even instruments geared toward 3-D reconstruction[26,41] typically have up to $\sim 10^3$ source–detector pairs, whereas our instrument utilizes 4×10^4 source–detector pairs per wavelength for reconstruction. The direct use of a lens-coupled CCD, as opposed to fiber coupling, greatly reduces the calibration coefficient unknowns. The parallel-plate transmission geometry with soft compression provides increased light transmission and reduced-detection dynamic-range linearity requirements compared to other geometries, e.g., the uncompressed conical or ring geometry. The use of Intralid/Ink fluids further reduces dynamic-range requirements and ensures good contact between optodes (sources and detectors) and the diffuse medium (i.e., the breast and Intralid/Ink fluid). Finally, our hybrid system permits measurement of bulk optical prop-

erties for use as initial guess in our reconstruction. Pure continuous-wave measurement systems[14,20] do not have this capability.

2.2 DOT Measurement Protocol

All human research was approved by the University of Pennsylvania Institutional Review Board. Informed consent was obtained from each subject. Then, the subject was positioned on the table with both breasts inside the empty breast box. Based on the tumor location identified by palpation or prior radiological information, the breast position with respect to the viewing window was optimized such that the tumor was well within the field of view. Then, a soft compression was applied to hold the breast in a stable position. The compression distance varied between 5.5 and 7.5 cm (6.4 ± 0.5 cm), depending on the breast size. A snapshot of the breast outline was taken by the CCD camera before filling the box with the Intralipid/Ink fluid. After filling the box, the diffuse optical image scan was conducted for $8-12$ min. Typically, we only measured a single breast per subject, most often with a single lesion. After the subject measurements, we filled the breast box completely with Intralipid/Ink fluid and covered the top of the box with a slab of silicone phantom to take reference optical measurements. The silicone slab extends the diffuse medium vertically above the breast box, just as the subject's torso extends the diffuse medium in the actual breast measurement.

2.3 3-D DOT Reconstruction

The NIR spectra of major tissue chromophores, such as oxygenated hemoglobin (HbO$_2$), deoxygenated hemoglobin (Hb), water, and lipid, are well-known,[49] and imaging is readily possible because their NIR absorptions are much lower than in visible or infrared spectral regions. The overall tissue absorption coefficient, μ_a, at a given wavelength (λ) may be decomposed into linear contributions from major chromophores via the relation $\mu_a(\lambda) = \sum_{l=1}^{L} \epsilon_l(\lambda) C_l + \mu_a^{bg}(\lambda)$, where L is the total number of chromophores, $\epsilon_l(\lambda)$ is the extinction coefficient of the lth chromophore, C_l is the concentration of lth chromophore, and μ_a^{bg} is a background absorption coefficient. The scattering coefficient is significantly larger than the absorption coefficient in the NIR, so that the propagation of light is well-modeled by the photon-diffusion equation.[50–52] The spectral variation of the reduced scattering coefficient is further approximated to have the form, $\mu_s'(\lambda) = A\lambda^{-b}$, a result based on simplified Mie scattering theory. Here, A is the scattering prefactor and b is the scattering power, which depends on the size and number of the scatterers in the tissue.[53,54] The multispectral method utilizes these spectral relations as constraints, using all wavelength data simultaneously to fit for chromophore concentrations and scattering factors directly, rather than first fitting μ_a and μ_s' individually for each λ and then subsequently calculating concentrations C_l.[45,46,55]

Using this multispectral method, we derived average bulk optical properties of breast based on remission frequency-domain measurements by fitting C_{Hb}^{bulk} (breast), $C_{HbO_2}^{bulk}$ (breast), A^{bulk} (breast), and b^{bulk} (breast) using an analytic solution of photon-diffusion equation for a semi-infinite medium. $\mu_a^{bg}(\lambda)$ of breast was fixed as a combination of 31% water and 57%

lipid absorption based on the literature.[56–58] Intralipid/Ink fluid properties C_{ink}^{bulk}, A^{bulk} (Intralipid), and b^{bulk} (Intralipid) were derived from frequency-domain reference measurements made on the breast box when it was completely filled with an Intralipid/Ink solution.

Then, we applied the multispectral approach to enhance image reconstruction by reducing the number of unknowns compared to the available measurements.[45,46] This approach enables us to achieve reasonable separation between absorption and scattering even for continuous-wave measurements. The unknowns for reconstruction were $C_{Hb}(\mathbf{r})$, $C_{HbO_2}(\mathbf{r})$, and $A(\mathbf{r})$, where $\mathbf{r}$ represents position within the 3-D sample volume. To assess the initial values for these parameters, we segmented the reconstruction volume into a half-ellipsoidal breast region and an Intralid/Ink fluid region based on the breast outline photo. Then, initial values for the parameters $C_{Hb}(\mathbf{r})$ and $C_{HbO_2}(\mathbf{r})$ were assigned to C_{Hb}^{bulk} (breast) and $C_{HbO_2}^{bulk}$ (breast) if $\mathbf{r}$ falls into the breast region or to zero otherwise. Initial values for $A(\mathbf{r})$ were set to A^{bulk} (breast) if $\mathbf{r}$ falls into the breast region or A^{bulk} (Intralipid) if it falls into Intralipid/Ink fluid region. μ_a^{bg} of the Intralipid/Ink fluid region was fixed by the directly measured μ_a of the fluid through C_{ink}^{bulk}. The scattering power was fixed as b^{bulk} (breast) and b^{bulk} (Intralipid) for each region, respectively.

For the given set of optical properties, a finite-element method based numerical solver[59] was utilized to derive a calculated fluence rate, $\Phi_c(\mathbf{r}_d)$ at detector position $\mathbf{r}_d$, given a set of optical properties. To suppress image artifacts associated with sources and detectors, we used a nonuniform, unstructured mesh with higher nodal concentrations at source/detector planes for the finite-element method.[60] The measured fluence rate, $\Phi_m(\mathbf{r}_d)$, was constructed by down-sampling and smoothing the CCD data on a 41×24 grid (as shown in Fig. 1) corresponding to a 3 mm spacing for each detector.

We defined a Rytov-type objective function χ^2 with the Intralid/Ink fluid reference measurements used for normalization (the specific form of χ^2 is given in Ref. 19 and in the Appendix). The unknowns were updated using an iterative conjugate-gradient-based scheme[61] modified to include the multispectral approach.[45,46] The iterative nonlinear method is superior to linear methods for quantification, because the inverse problem is intrinsically nonlinear. The memory-efficient conjugate gradient method allowed use of large data sets (10^4 spatial $\times 6$ spectral data). Furthermore, parallel computation was implemented to dramatically speed up reconstruction time.

In order to compensate for higher sensitivity near source/detector planes and lower sensitivity near the sample center, spatially variant regularization[62] was added within the objective function. To find an optimum regularization parameter, α, an initial reconstruction using an envelope-guided regularization technique[63] was performed, first yielding an estimate of the initial regularization parameter, α_0.[64] Then, nine reconstructions were performed with nine different regularization parameters ranging from $0.01\alpha_0$ to $100\alpha_0$ to further optimize this parameter. We examined the L curve that plots the residual norm (i.e., the sum squared difference between measured and calculated data) versus the image norm (i.e., the sum squared difference between the initial guess and recon-

structed optical parameters) to find the optimal regularization parameter.

After the selection of the best $C_{Hb}(\mathbf{r})$, $C_{HbO_2}(\mathbf{r})$, and $A(\mathbf{r})$ images based on the optimal regularization parameter determined by the *L*-curve analysis, we constructed 3D images of total hemoglobin concentration $[\text{THC}(\mathbf{r})=C_{Hb}(\mathbf{r})+C_{HbO_2}(\mathbf{r})]$, blood oxygen saturation $[\text{StO}_2(\mathbf{r})=C_{HbO_2}(\mathbf{r})/\text{THC}(\mathbf{r})]$, scattering $\mu_s'(\mathbf{r},\lambda)=A(\mathbf{r})\lambda^{-b(\mathbf{r})}$, and the overall optical attenuation $\mu_{\text{eff}}(\mathbf{r})=\sqrt{3\mu_a(\mathbf{r})\mu_s'(\mathbf{r})}$ at 786 nm.

2.4 Extraction of DOT Tumor Parameters

In order to extract DOT parameters from tumor and healthy regions, additional steps were taken. First, the approximate tumor location was determined based on MR images of the same breast. Each tumor was classified as belonging to the retroareolar region or one of four quadrants (i.e., upper outer, upper inner, lower inner, and lower outer quadrant). The relative proximity of the mass with respect to the nipple and the chest wall was also noted. When MRI was not available, spatial information about the tumor was derived from radiology reports based on X-ray mammograms and ultrasound. Then, based on the outline photo of the breast, we determined the position of the nipple in the DOT images and then in the corresponding axial DOT slices. We chose to use a μ_{eff} at 786 nm map for tumor segmentation, as it represents a combination of absorption and scattering contrast and, therefore, is less sensitive to parameter cross-talk.

The spatial location with maximum intensity of μ_{eff} at 786 nm near the radiologically determined tumor region was marked as the starting point for a 3-D region growing algorithm, with cutoff at full-width-at-half-maximum. When the tumor-to-normal contrast was relatively low, such that the region grew into multiple locations, tumor size extracted either from pathology or radiology reports was used as a limiting factor to stop the growth algorithm. This approach was effective for selection of tumor regions in images while minimizing the influence of artifacts. Because our DOT reconstructions are subject to source and/or detector artifacts, slices near the source and detector planes (up to 8 mm) were excluded from the region-growing process. When the tumor was not adequately visible in DOT [e.g., in some fibroadenomas ($N=3$), lobular carcinomas *in situ* ($N=2$), and fibrocystic lesions ($N=1$)], then the lesion region was fixed based on radiological assessment rather than the region-growing algorithm. Normal tissue was defined as the breast tissue outside the tumor region based on the following criteria: (i) slices up to 8 mm from source and detector planes were excluded and (ii) regions with μ_{eff} at 786 nm outside plus/minus two standard deviations from its average over the entire breast were excluded. These exclusions ensured that source and detector artifacts were removed from the "average" normal tissue. Factors such as different compression schemes and shifts of nipple location due to breast-positioning variation were necessarily considered, because the breast is a highly deformable organ. MRI, for example, used sagittal compression for breast imaging, whereas DOT used axial compression in this study. We averaged the DOT parameters inside the regions defined by the above segmentation (i.e., to obtain mean $\bar{X}_{(T)}$ for the tumor region and mean $\bar{X}_{(N)}$ for the normal region,

Table 1 Definition of extracted optical parameters from DOT images. $\bar{X}_{(T)}$ and $\bar{X}_{(N)}$ are the mean values of variable X within the tumor region and normal region, respectively. OI is constructed based on these tumor-to-normal ratios of optical parameters.

Parameters	Abbreviation	Definition
Relative total hemoglobin concentration	$r\text{THC}$	$\overline{\text{THC}}_{(T)}/\overline{\text{THC}}_{(N)}$
Relative blood oxygen saturation	$r\text{StO}_2$	$\overline{\text{StO}_2}_{(T)}/\overline{\text{StO}_2}_{(N)}$
Relative deoxy-hemoglobin concentration	$r\text{Hb}$	$\overline{\text{Hb}}_{(T)}/\overline{\text{Hb}}_{(N)}$
Relative oxy-hemoglobin concentration	$r\text{HbO}_2$	$\overline{\text{HbO}_2}_{(T)}/\overline{\text{HbO}_2}_{(N)}$
Relative scattering coefficient (786 nm)	$r\mu_s'$	$\overline{\mu_s'}_{(T)}/\overline{\mu_s'}_{(N)}$
Optical index	OI	$r\text{THC}\times r\mu_s'/r\text{StO}_2$

(T): tumor, (N): normal

where X is the optically derived physiological variable). An optical contrast ratio (i.e., rX, the relative value of X between the tumor and normal tissue) was then defined as in Table 1. We also defined an optical index $\text{OI}=r\text{THC}\times r\mu_s'/r\text{StO}_2$. The rationale for this index was based on the hypothesis that tumor THC and scattering increase due to increased angiogenesis and cell proliferation, while StO_2 decreases due to hypermetabolism.[25] Images of relative values of any variable are defined in a similar fashion: $rX(\mathbf{r})=X(\mathbf{r})/\bar{X}_{(N)}$ and $\text{OI}(\mathbf{r})=r\text{THC}(\mathbf{r})\times r\mu_s'(\mathbf{r})/r\text{StO}_2(\mathbf{r})$.

2.5 Classification of Groups

Only the biopsy-proven lesions from the histopathology report were selected for quantification of optical tumor-to-normal contrast. Lesions were separated into three groups: benign (all benign lesions were measured by DOT before core biopsy), malignant lesions measured before core biopsy (Mal-Bcb), and malignant lesions measured after core biopsy (MalAcb). The separation of malignant lesions into pre- and post-core biopsy groups enabled us to address the concern that bleeding induced by core biopsy might influence DOT. Subjects who had fine needle aspiration prior to DOT measurements were included in the pre-core biopsy group (i.e., Mal-Bcb group), because the fine needle aspiration was deemed to have minimal effect. For the MalAcb group, the DOT measurement was carried out more than 1 week after core biopsy, ensuring some level of healing.

From demographic information, parameters such as age, height, weight, menopausal status, and race were also collected. Body mass index (BMI) was calculated as BMI $=\text{weight}/\text{height}^2$ (in kilograms per meters squared). From the pathology reports, in addition to lesion type, lesion size and modified Bloom and Richardson scores (mBR) were extracted. When the lesion size was not available or was ambiguous in the pathology report, the longest dimension of the

lesion was extracted from the radiology report and was taken as the lesion size. Mammographic density information was collected from the radiology reports.

2.6 *Statistical Analysis*

Statistical analysis of these data was performed using R 2.6, a statistical computing and graphics software.[65] A type I error rate of 0.05 was used for all hypothesis tests. Demographic data were summarized using means and 95% confidence intervals (CIs) for continuous data or percentages for categorical data.

The optical tumor contrast ratios were log-transformed to achieve approximate normality and then analyzed using a mixed-effects model.[65,66] In this model, we took into account the potential correlation between measurements taken from multiple lesions in the same breast or in the same women. We fit to a model that estimated the mean optical contrast ratio for each group. After developing 95% CIs using the resulting standard errors, we tested the hypothesis that each optical contrast parameter was unity. Because the bleeding induced by a core biopsy might be expected to influence DOT results, for the malignant group we tested the hypothesis that there were no differences in mean optical contrast ratio associated with receiving/not receiving a core biopsy. Also, we tested another null hypothesis that there were no differences in mean optical contrast ratios between benign and malignant groups. Finally, we used univariate models to test whether there was an association between optical tumor contrast ratios and clinical covariates including BMI, menopausal status, lesion size, and race. For any variable that showed a significant univariate association, we tested whether the association persisted in a model that also included lesion pathology (i.e., benign or malignant).

Lastly, to assess the capacity of the approach to discriminate between benign and malignant lesions, we constructed logistic regression models using each optical parameter as the predictor in the model. Odds ratios (ORs) were used to estimate the effect sizes, the significance of each effect was assessed using a Wald test, and an ROC curve was constructed using the estimates of sensitivity and specificity.[67] An AUC was calculated for each DOT parameter to serve as a measure of discrimination. Because logistic regression assumes that observations are independent, we carried out a sensitivity analysis using a subset of the data where the malignant lesions from two women with a benign lesion were dropped, and where one malignant lesion was dropped from each of the two women with two malignant lesions. This modification to the data set had negligible impact on the findings presented here. Representative error estimates for sensitivity and specificity were computed using the exact binomial distribution.

3 Results

3.1 *Demographic, Radiologic, and Histopathologic Information of Benign and Malignant Lesions*

We recruited 60 female subjects for DOT measurement between the years 2001 and 2006. All of these subjects had a clinically suspicious lesion. Subjects with prior mass-removal surgery ($N=4$) or subjects undergoing neoadjuvant chemotherapy ($N=2$) were not included in the analysis. Thus, only properties of lesions prior to clinical intervention were

Table 2 Clinical characteristics of subjects, categorized by benign or malignant lesions. For continuous data such as age, mean±standard deviations are shown. For each categorical variable, the number of women is shown. The percent of the total number of women in the group appears in parentheses.

Parameters	Subjects with benign lesions ($n=10$)	Subjects with malignant lesions ($n=37$)
Age (yr)	43±11	48±11
BMI (kg/m^2)	26±5	27±6
Menopausal status		
Premenopausal	6 (60%)	19 (51%)
Postmenopausal	4 (40%)	18 (49%)
Race		
Caucacian	7 (70%)	29 (78%)
African American	1 (10%)	6 (16%)
Asian	1 (10%)	1 (3%)
Hispanic	1 (10%)	1 (3%)
Mammographic density		
Almost entirely fat	1 (10%)	2 (5%)
Scattered fibroglandular densities	3 (30%)	9 (24%)
Heterogeneously dense	3 (30%)	20 (54%)
Extremely dense	1 (10%)	1 (3%)
Unknown	2 (20%)	5 (14%)
Lesion size (cm)	1.8±1.7	2.1±1.2

probed. Subjects with breast implants ($N=1$) or with extensive bleeding due to previous core biopsy ($N=2$) were also excluded from the analysis, because these conditions significantly affected DOT signal-to-noise. Subjects with no biopsy results ($N=4$) were excluded as well. We report on DOT measurements and analyses of 47 female subjects with biopsy-proven lesions.

Fifty-one lesions from 47 patients were characterized with DOT. Ten patients had benign lesions, and of these, two patients had an additional malignant lesion. In Table 2, these patients were assigned to the benign group. A total of 37 patients had exclusively malignant lesions, and of these, two patients had two lesions. No patient had more than two lesions. The demographic information for patients in benign and malignant groups is presented in Table 2. Average lesion size along the longest dimension was 1.8 cm for benign and 2.1 cm for malignant lesions, ranging from 0.4 to 9.3 cm. The majority of women in this study were premenopausal (60% of benign group, 51% of malignant group) and Caucasians ($>65\%$ both groups) with mean ages of 43 (benign group) to 48 (malignant group). At least half of both groups

Table 3 Pathologic characteristics of 51 lesions measured with DOT before or after core biopsy.

Histopathologic diagnosis	Number of lesions measured by DOT before core biopsy ($n=30$)	Number of lesions measured by DOT after core biopsy ($n=21$)
Malignant ($n=41$)		
Invasive ductal carcinoma	16	20
Invasive lobular carcinoma	2	0
Ductal carcinoma *in situ*	2	1
Benign ($n=10$)		
Fibroadenoma	4	0
Cyst	3	0
Fibrocystic	1	0
Lobular carcinoma *in situ*	2	0

with known mammographic density had heterogeneously dense or extremely dense breasts as determined by X-ray mammography.

The histopathologic diagnosis of these lesions is summarized in Table 3. We divided the 51 lesions into three groups: (i) benign, (ii) MalBcb, and (iii) MalAcb. 80 and 95% of the malignant lesions measured before and after core biopsy in this study were invasive ductal carcinoma, while 40% of the benign lesions were fibroadenomas, 30% were cysts, 30% were lobular carcinoma *in situ*, and 10% were fibrocystic disease.

3.2 Example Images of MRI and DOT

Three representative DOT images are shown in Figs. 2–4. Figures 2(a)–2(c), 3(a)–3(c), and 4(a)–4(c) provide three images: one sagittal DCE-MR image slice at the tumor center, an axial DCE-MR image slice along the horizontal line drawn in the sagittal image, and a 3-D depiction of the breast outline and tumor region. The axial MRI slice was rearranged such that the orientation matches with DOT orientation (i.e., caudal-cranial). The DOT slices are arranged to show rTHC($\mathbf{r}$), rStO$_2$($\mathbf{r}$), rHbO$_2$($\mathbf{r}$), rHb($\mathbf{r}$), and $r\mu_s'$($\mathbf{r}$) at 786 nm and OI($\mathbf{r}$) along the horizontal line. In order to help with comparison, the color-bar range was fixed throughout the examples for each parameter (e.g., 0.8–1.3 for rTHC and 0.6–2.1 for OI).

Clear distinctions between the lesion and surrounding tissue were observed in rTHC, $r\mu_s'$, and OI images for the invasive carcinoma (Fig. 2). Intermediate contrasts were observed for the ductal carcinoma *in situ* (Fig. 3) and low contrasts for the fibroadenoma (Fig. 4).

3.2.1 Invasive ductal carcinoma

The first example is from a 53-year-old postmenopausal female with a retroareolar mass in her right breast. DOT measurements were performed before any core biopsy. Dynamic contrast enhanced MR images showed a clear enhancement of Gadolinium uptake signal behind the nipple in Fig. 2. The size

of the enhancement determined by radiologists was 2.2 cm. The mammographic density of this breast fell into the scattered fibroglandular category. Histopathology analysis after mastectomy revealed a 2.0-cm mixture of invasive ductal carcinoma (with mBR grade of 8) and ductal carcinoma *in situ* behind the nipple.

The compression distance for the DOT measurement of the same subject was 6 cm. The nipple was shifted toward the source plane during DOT positioning; thus, the slice best exhibiting the tumor contrast turned out to be the one 1.8 cm away from the source plane. As can be seen in Fig. 2, DOT slices showed elevated rTHC, $r\mu_s'$, rHbO$_2$, rHb, and OI at the tumor site, slightly displaced toward the lateral side (i.e., the right side of the axial image for right breast), in agreement with the MRI axial slice. The rStO$_2$ slice did not exhibit a localized feature, but rather it showed a broad, slightly low oxygenation region near the tumor location. While elevated values of most parameters were apparent within the tumor site, subtle differences in the images were always found.

3.2.2 Ductal and lobular carcinoma in situ

The second example is from a 39-year-old premenopausal female with a mixture of ductal carcinoma *in situ* and lobular carcinoma *in situ* in her left breast. X-ray mammography and ultrasound detected a 3-cm mass at 3 o'clock. In DCE-MRI, enhancement spanning 3–5 cm appeared around 3–4 o'clock, which corresponds to left upper side of the axial image as shown in Fig. 3(b). DOT measurements were performed before core biopsy. The mammographic density of this breast fell into the extremely dense category. Histopathology analysis of the excisional biopsy sample revealed an extensive ductal carcinoma *in situ*, with intermediate-grade nuclei growing in a solid pattern with focal comedo-type necrosis and extensive lobular carcinoma *in situ*.

The compression distance for the DOT measurement was 6 cm. The nipple was shifted toward the detector plane during DOT positioning; thus, the slice at 4.6 cm from the source plane was selected for presentation. In the reconstructed im-
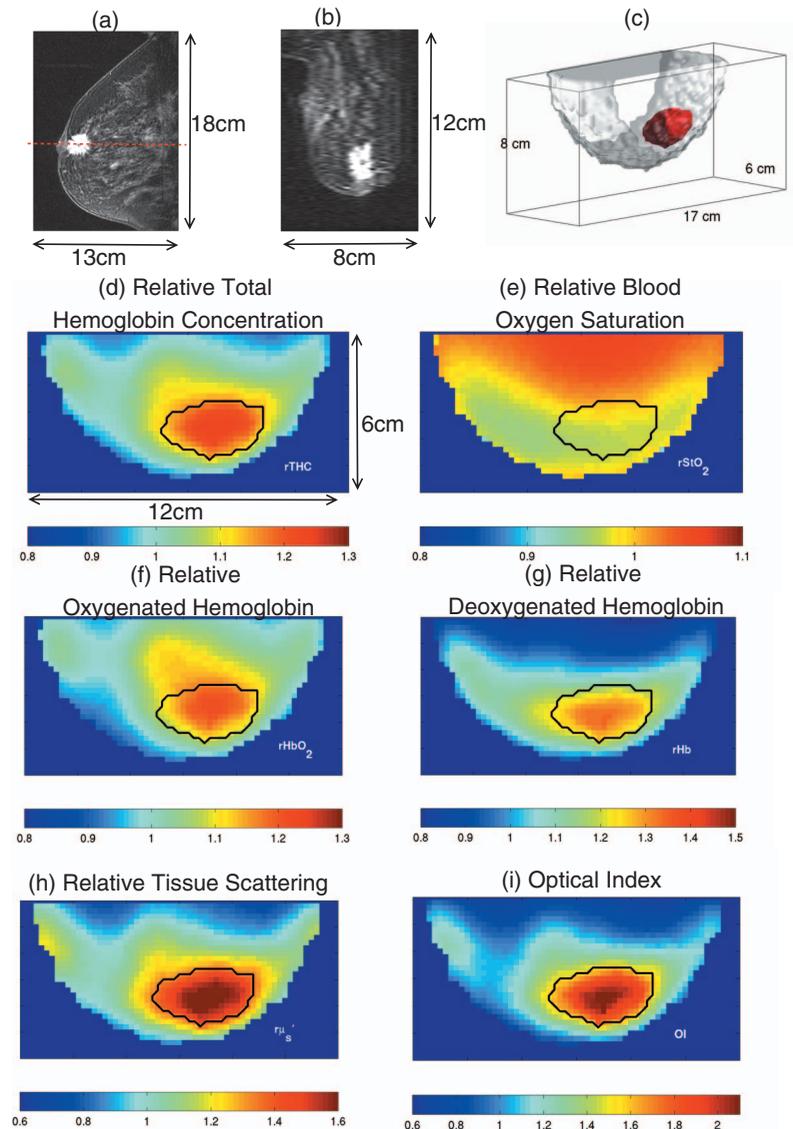
Fig. 2 MR image and DOT image of a 53-year-old woman with a 2.2-cm invasive ductal carcinoma in her right breast. (a) is the sagittal dynamic-contrast-enhanced (DCE) MRI containing the tumor center, (b) is the axial DCE MRI slice along the red horizontal line in (a), oriented in caudal-cranial view. Enhancement of gadolinium uptake in MRI indicates the malignancy. (c) depicts the tumor region (in red) determined based on optical data with the guidance of MRI and the breast outline (in pink) in three-dimensional space. DOT images of (d) relative total hemoglobin concentration rTHC, (e) relative blood oxygen saturation rStO$_2$, (f) relative oxygenated hemoglobin concentration rHbO$_2$, (g) relative deoxygenated hemoglobin concentration rHb, (h) relative tissue scattering $r\mu_s'$ at 786 nm and (i) OI are shown in caudal-cranial view with a black solid line indicating the region identified as tumor using a region-growing algorithm. High tumor-to-normal contrast in rTHC, rHbO$_2$, rHb, $r\mu_s'$, and OI are visible within the region.

ages (Fig. 3), three regions with elevated contrast in rTHC and $r\mu_s'$ are evident. However, the contrast of each region is much lower than those of the invasive carcinoma shown in Fig. 2. The left upper region corresponding to the tumor site exhibited high optical contrast in rTHC, $r\mu_s'$, and OI. The lower center region corresponds to the nipple showing rTHC, $r\mu_s'$, and OI larger, and rStO$_2$ smaller than unity.

3.2.3 *Fibroadenoma*

The third example is from a 51-year-old premenopausal female with a fibroadenoma in her left breast. DCE-MRI saw asymmetric density exhibiting some enhancement in the lower outer quadrant [as seen in Fig. 4(b) at the left upper

side]. However, no suspicious finding was identified by ultrasound or from the digital mammogram. DOT measurements were performed before any core biopsy. The mammographic density of this breast was categorized as scattered fibroglandular density. Needle localization biopsy yielded benign breast tissue with a 5 mm fibroadenoma.

In the reconstructed images (from a slice 4.6 cm away from the source plane) of Fig. 4, distinct optical contrast in the expected region was not found. The compression distance for the DOT measurement was 6.5 cm. Because the optical contrast was not apparent, a spherical region was assigned as a benign lesion in DOT images based on the extent of gadolinium enhancement in the DCE-MR image, which was sub-
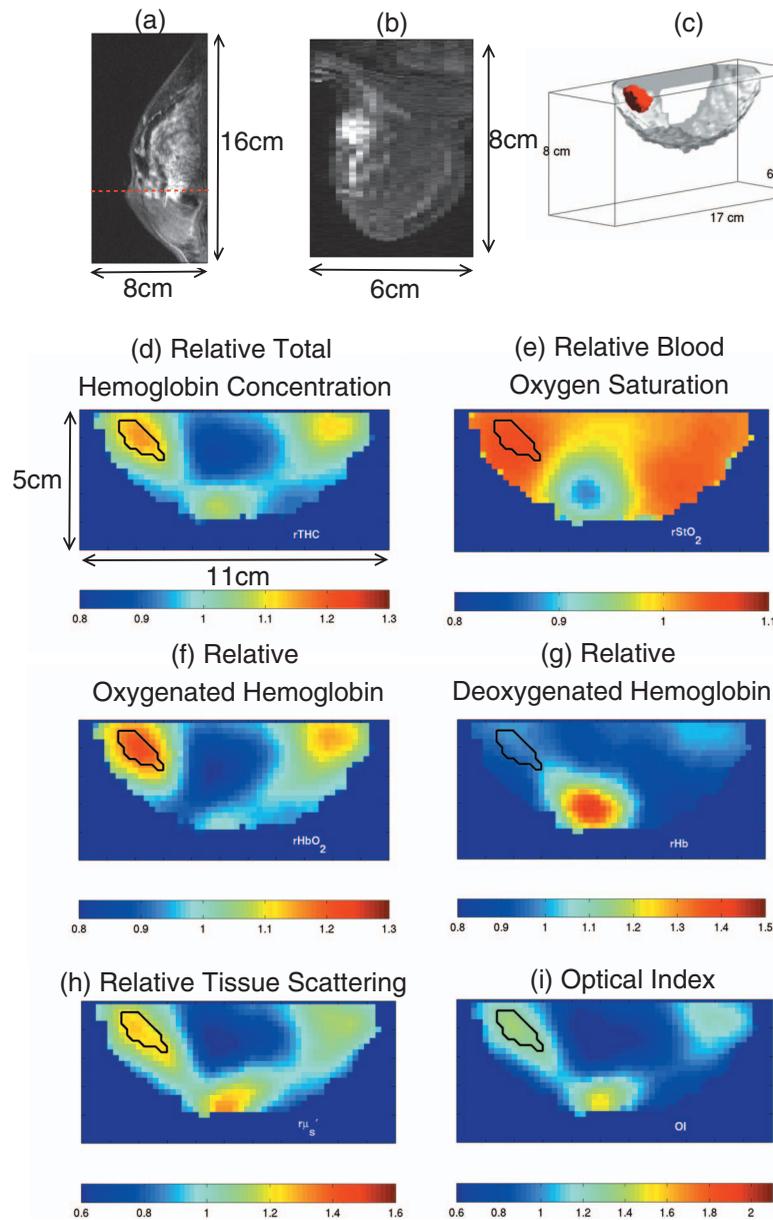
Fig. 3 MR image and DOT image of a 39-year-old woman with ductal and lobular carcinoma *in situ* spanning $3-5$ cm in her left breast. The axial DCE-MR image shows enhancement at the lesion. The black solid line indicates tumor region determined by a region growing algorithm based on this information from MRI. DOT images show elevated rTHC, rHbO$_2$, $r\mu_s'$, and OI in tumor region compared to the surrounding tissue.

stantially larger than the size reported by histopathology. Two regions of high OI were notable, but they did not correspond to the fibrosis region identified by MRI.

3.3 Distinction between Benign and Malignant Lesions Based on Optical Tumor Contrast

Figure 5 shows the data for each group, while Table 4 summarizes mean values and 95% confidence intervals for optical contrast parameters (rTHC, rStO$_2$, $r\mu_s'$, rHb, rHbO$_2$, OI). A value of 1.0 indicates zero contrast. The benign group exhibited contrast of $0.96-1.11$ for all parameters, which was not significantly different from 1.0. With the exception of rStO$_2$, the parameter estimates for the malignant lesions in both Mal-Bcb and MalAcb groups were significantly higher than 1.0.

Mean values of $r\mu_s'$ and OI were more than 1.5 and 1.8 for both malignant groups. In no case were significant differences found between mean values of the parameters for the MalBcb and MalAcb groups. The intrasubject tissue variability (σ_Y/Y) was calculated based on the standard deviations of both normal (N) and tumor (T) regions, i.e., $\sigma_Y/Y = \sqrt{(\sigma_{X_{(N)}}/\bar{X}_{(N)})^2 + (\sigma_{X_{(T)}}/\bar{X}_{(T)})^2}$, where $Y = \bar{X}_{(T)}/\bar{X}_{(N)}$. The median intrasubject variability of 51 lesions for rTHC, rStO$_2$, $r\mu_s'$, rHb, and rHbO$_2$ were 9, 5, 20, 10, and 14%, respectively. This intrasubject variability for each region was not included in the statistical analysis presented in Table 4, because the focus of the current study was not the automatic detection of the lesion location but rather the characterization
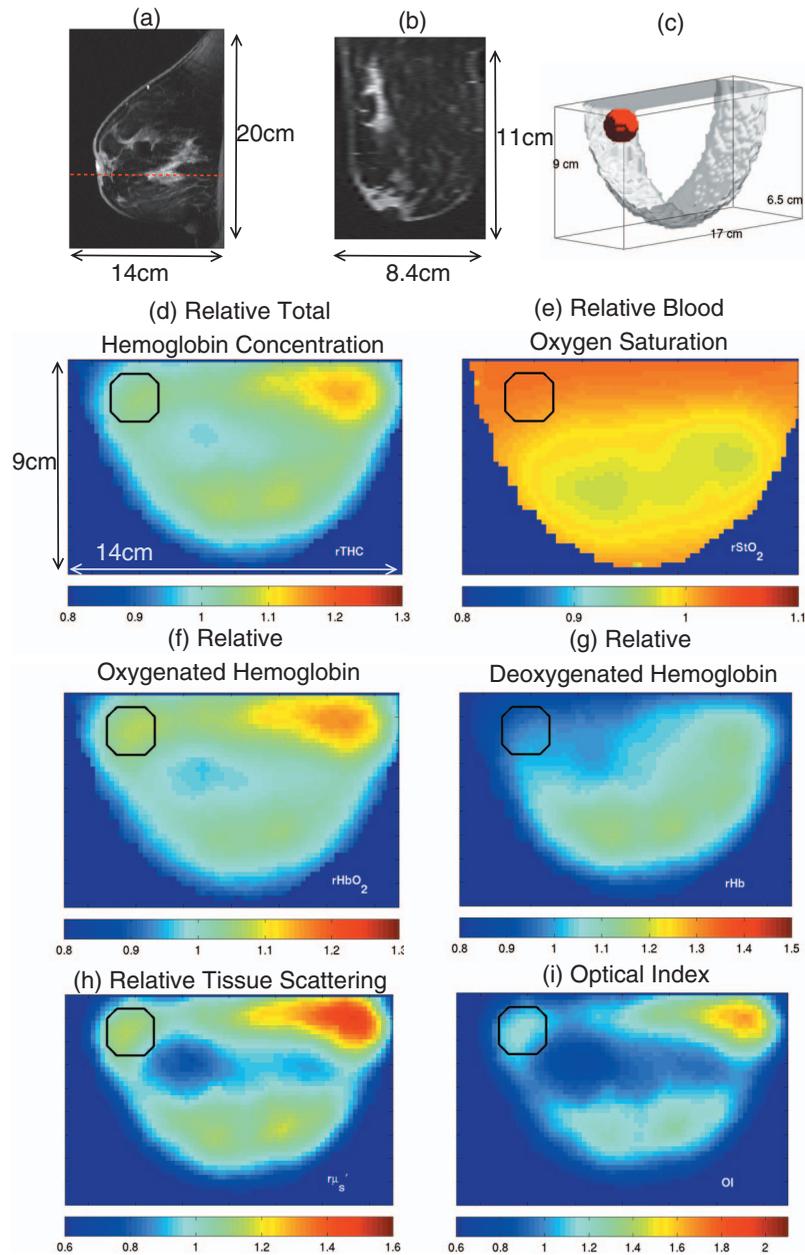
Fig. 4 MR image and DOT image of a 51-year-old woman with a 5-mm fibroadenoma in her left breast. The DCE-MR image shows an asymmetric density exhibiting some enhancement in lower outer quadrant. Because the optical contrast was not apparent, a spherical region was assigned as a benign lesion in DOT images (black solid line) based on the extent of gadolinium enhancement in DCE-MR image. Tumor-to-normal contrast in all parameters and OI are similar to that of surrounding tissue.

of lesions, with lesion location provided by other imaging modalities. Menopausal status, race, and size of lesion did not show an association with any of the optical contrast parameters (data not shown). However, BMI was associated ($P < 0.05$) with both $r\mu_s'$ and OI in both univariate models and after adjustment for type of lesion (malignant versus benign). While the effects of BMI were statistically significant for $r\mu_s'$ and OI, they were substantially less than the effects of lesion type (data not shown).

Figure 6 shows the ROC curves for rTHC, rHbO$_2$, $r\mu_s'$, and OI. The ROC curves plot the true positive rate on the vertical axis and the false positive rate on the horizontal axis.

For example, for rTHC, if we designated a lesion with rTHC > 1.06 as malignant, then 40 out of 41 malignant lesions would be correctly identified for a sensitivity (true positive rate) of 98% (95% CI=87–100%), and 9 out of 10 benign lesions would be correctly identified for a specificity (1− false positive rate) of 90% (95% CI of wide range: 55–100%). Table 5 shows the AUC and OR values for a lesion to be malignant versus benign for each optical parameter. All of the parameters except rStO$_2$ and rHb were positively associated with increased odds of malignancy, with OR values ranging from 4.3 to 176 per 0.10 (10%) increase in the relative optical parameters. Similarly, the AUCs suggested good discrimina-
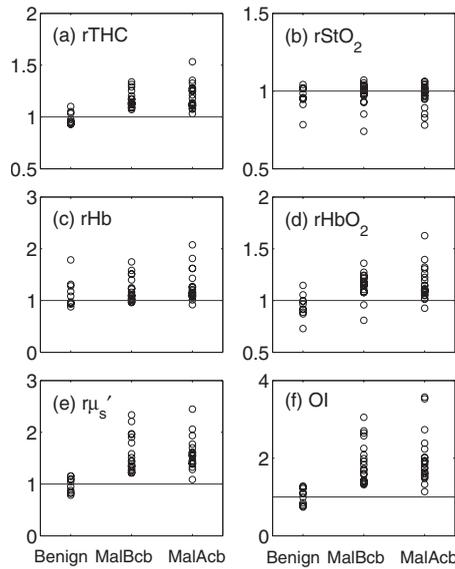
Fig. 5 rTHC, rStO$_2$, $r\mu_s'$, rHb, rHbO$_2$, and OI of all 51 lesions. Lesions are separated into three groups: benign lesions, malignant lesions measured before core-biopsy (malBcb), and malignant lesions measured after core-biopsy (malAcb).

Fig. 6 Receiver operating characteristic curves for rTHC, rHbO$_2$, $r\mu_s'$, and OI showing true positive rate for malignant lesions versus false positive rate for benign lesions. These rates are calculated by imposing a cutoff value (i.e., numerical values on each curve). For example, if rTHC > 1.06 designates positive result, then true positive rate is 98% and false positive rate is 10%.

tory power with values, excluding rStO$_2$ and rHb, between 0.90 and 0.99. The OR values for rTHC, $r\mu_s'$, rHbO$_2$, and OI achieved statistical significance (i.e., $P < 0.05$). However the 95% CIs of ORs were wide. For example, the 95% CI for $r\mu_s'$ was from 1.4 to 333, the 95% CI for rTHC was from 3.3 to 9432, and the 95% CI for OI was from 1.3 to 33.3. This indicates substantial uncertainty in the parameter estimates and is a result of the relatively small sample size, particularly the small number of benign lesions ($N = 10$). Additionally, the performance of any of these predictors would weaken if applied to a new validation dataset, because the predictions are based on a small number of benign lesions.
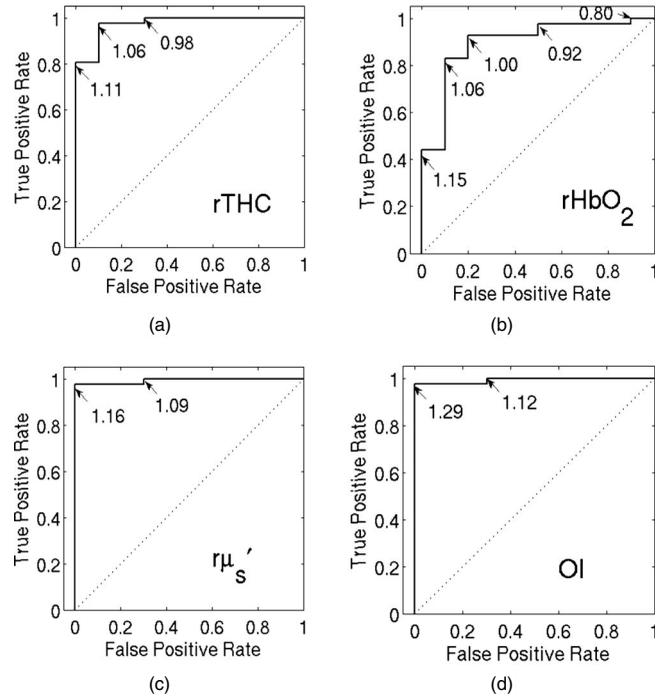
4 Discussion

4.1 Significance

Several groups have reported measurable differences in the optically-derived properties of breast tumors compared to background tissues.[11–14,17,21–24,41] The research reported herein, however, differs for several reasons, including instru-

Table 4 Mean (95% CI) of extracted relative DOT parameters for three different lesion groups and P values testing three different types of hypotheses. P_a is the measure for the difference between tumor and normal tissue. P_b is the measure for the difference between malignant groups measured before (MalBcb) and after core biopsy (MalAcb). P_c is the measure for the difference between benign and malignant groups. An asterisk indicates that the difference is statistically significant ($P_x < 0.05$).

	Benign		Malignant before core biopsy		Malignant after core biopsy		Biopsy effect	Benign versus Malignant
Parameter	mean (95% CI)	P_a	mean (95% CI)	P_a	mean (95% CI)	P_a	P_b	P_c
rTHC	0.98 (0.89–1.09)	0.56	1.16 (1.08–1.25)	0.01*	1.19 (1.10–1.28)	0.01*	0.45	0.01*
rStO$_2$	0.96 (0.86–1.08)	0.27	0.98 (0.90–1.06)	0.38	0.97 (0.90–1.05)	0.22	0.71	0.13
rHbO$_2$	0.94 (0.80–1.11)	0.25	1.14 (1.01–1.28)	0.04*	1.15 (1.03–1.29)	0.03*	0.79	0.02*
rHb	1.11 (0.85–1.45)	0.23	1.18 (0.98–1.43)	0.06	1.24 (1.03–1.49)	0.04*	0.54	0.32
$r\mu_s'$	0.98 (0.77–1.25)	0.79	1.53 (1.28–1.83)	0.01*	1.53 (1.28–1.84)	0.01*	1.00	0.005*
OI	1.04 (0.76–1.41)	0.67	1.83 (1.43–2.35)	0.01*	1.84 (1.43–2.37)	0.01*	0.96	0.004*

Table 5 AUC and OR of lesion being malignant versus benign for a 0.10 (10%) increase in the value of the optical parameter. Asterisks are associated with $P < 0.05$ to indicate statistical significance.

Parameter	AUC	OR (95% CI)	P
rTHC	0.98	176 (3.3–9432)	0.01*
rStO$_2$	0.57	1.3 (0.5–3.0)	0.61
rHbO$_2$	0.90	4.3 (1.7–10.7)	0.001*
rHb	0.66	1.2 (0.9–1.7)	0.27
$r\mu_s'$	0.99	21.4 (1.4–333)	0.03*
OI	0.99	6.5 (1.3–33.3)	0.03*

mentation, 3-D image reconstruction, and lesion definition (i.e., MRI-guided).

Perhaps most importantly, our results correlate DOT and DCE-MRI in a significant number of subjects. Other groups have demonstrated the correlation of the stand-alone DOT data with X-ray mammograms and/or ultrasound,[13,21,22,29,68,69] or less frequently with MRI[37,48] for a limited number of subjects. Some groups have measured concurrently with other imaging modalities: MRI,[11,70–72] ultrasound,[17,27] and 3-D tomosynthesis.[73,74] However, most of these concurrent results rely heavily on *a priori* spatial information from the other imaging modality for 3-D optical reconstruction. Our ability to reconstruct accurate images without *a priori* spatial information is due to our DOT instrumentation and reconstruction algorithms which were designed to provide and utilize the large data sets essential for full 3-D reconstruction. The number of on-axis and off-axis measurements of our lens-coupled CCD detection is the largest among existing 3-D DOT instruments[13,14,16,17,20,21,48] (i.e., larger by factors of $\sim 100 \times$ or more before downsampling). The 3-D DOT reconstructions are based on measurements at multiple optical wavelengths chosen to better separate scattering from absorption and isolate individual chromophore contributions.[45,46] Furthermore, the use of DCE-MR images and radiology reports enable us to better define tumor margins and locations in the diffuse optical images, in some cases reducing ambiguities that would be present had we employed the optical images alone. With these features, we demonstrated a clear distinction between benign and malignant tumor optical properties with statistical significance.

4.2 Comparison of DCE-MRI and DOT Images

DCE-MRI using gadolinium-diethylene triamine pentaacetic acid stands out among clinical imaging modalities by offering vasculature-sensitive parameters.[75,76] It is therefore a good choice for comparison to DOT. Sometimes tumor contrast is clear in both DCE-MRI and in most parameters of DOT (Fig. 2), while the DOT contrast from benign lesions is often negligible (Fig. 4). Furthermore, in some cases, more than one high-contrast region appears in the DOT images (Figs. 3 and 4). Sometimes these high-contrast regions are identified as the nipple or as glandular tissue positioned near the detector plane and are also seen in DCE-MRI. These regions exhibit subtle spatial differences among parameters (e.g., the shape or the center of the contrast region) or distinct characteristics when all the parameters are considered together. For example, the nipple in Fig. 3 exhibited lower blood oxygen saturation, whereas the ductal carcinoma *in situ* showed higher StO$_2$ than the surrounding tissue; both exhibited values higher than unity for rTHC, $r\mu_s'$, and rHbO$_2$. Some high-contrast regions in DOT reconstructions are not found in DCE-MRI (e.g., Figs. 3 and 4); these regions could be tissue with a physiologically elevated level of hemoglobins/scattering (but insensitive to DCE-MRI), or they could be DOT image artifacts. Further work is needed to classify these regions and to devise image-processing constraints to reduce image artifacts. For now, we have focused our efforts on characterization of tumor-to-normal ratio in order to derive upper bounds about what can be done with optics.

4.3 Relative Measures and the Optical Index

Our focus on tumor-to-normal ratios rather than absolute properties is driven by the observation that intersubject absolute optical property variation is quite significant. For example, averaged over the whole breast, reconstructed THC varied from 6 to 45 μM and reconstructed μ_s' at 786 nm from 7 to 13 cm^{-1}. Intersubject variation in absolute optical properties is caused by differences in breast-tissue composition. A significant inverse correlation between THC and BMI has been found, for example, across a wide range of DOT/DOS instrumentation and measurement geometries.[21,55,77,78] Higher BMI is indicative of more adipose tissue content, wherein the blood supply is smaller than in glandular tissue.[34] In contrast to absolute THC, rTHC has emerged from our data as robust quantity for tumor contrast regardless of tissue composition. Similarly, $r\mu_s'$ has proven superior to absolute μ_s' for tumor contrast. Evidently relative contrast can remain, even if absolute optical properties shift. It is also desirable to find other tissue optical indices which improve malignancy contrast. This concept has also been used by Cerussi et al..[40] Our suggested optical index, OI $= r$THC $\times r\mu_s'/r$StO$_2$, improved tumor contrast and is a logical composite variable based on the hypothesis of tumor hypermetabolism.[25] It is also less sensitive to absorption-scattering crosstalk.

4.4 Physiological Origins of Optical Tumor Contrast

Angiogenesis associated with solid tumors of radiologically detectable size[79] likely contributes to high THC contrast between breast tumor and normal tissue measured by DOT. DOT is sensitive to vasculature at the microvessel level (i.e., capillaries, arterioles, and venules). Indeed, a positive correlation between microvessel density and THC has been found, providing further insight about the microscopic origin of THC contrast.[13,27,28] Among various physiological parameters available to DOT and DOS, most groups have reported the high THC contrast of malignant tumors.[13,14,17,18,21,26,28,80–83]

The origin of scattering contrast of the cancer is more elusive than absorption. Nevertheless, an increase in number density of subcellular organelles (e.g., mitochondria and nucleolus), due to cell proliferation, can increase tissue scattering. Recently, Li et al.[29] have observed significant differences in the mean size and volume fraction of cellular scattering components (thus scattering coefficients) between

benign and malignant lesions. Some groups have reported tumor scattering contrast comparable to ours,[29] and some have reported contrast ~20–40% higher than normal tissue scattering.[23,28,81,82] Because of absorption and scattering crosstalk issues, at the present time there remains some uncertainty about the fidelity of the scattering assignment. In our laboratory, we have shown that it is possible to decouple chromophore concentrations and scattering in continuous-wave data by choosing optimal wavelengths.[45,46] However, our current system does not utilize all the optimal wavelengths. According to simulations using the experimental wavelength set, reconstructed rTHC was often underestimated, while $r\mu_s'$ was often overestimated by 10–20% (data not shown). The overall influence on the optical index was a 10% underestimation. Thus, even though our wavelengths were suboptimal, the resulting parameter crosstalk does not appear to influence the major findings of this study.

Our measurements of StO_2 contrast were not compelling. Cancer oxygen metabolism may depend strongly on the cancer stage and biochemical pathways involved. Also, changes in blood oxygenation may be subtle compared to changes in tissue oxygenation induced by tumor hypermetabolism. Indeed, some groups have observed a decrease of StO_2 in the tumor,[25,26,84–87] whereas others observed no difference[21,23,24,40,88] or even an increase.[81]

Images of cancer metabolism have been widely utilized in the positron emission tomography community, wherein breast cancer is frequently characterized by hyperglucose metabolism measured by increased uptake of fluorine-18 fluorodeoyglucose (^{18}F-FDG).[89,90] The potential connection between glucose metabolism and oxygen metabolism of cancer may exist; for example, we observed a positive correlation between the uptake of FDG and rTHC, $r\mu_s'$ and OI using a subset of the present data.[91] Thus far, however, DOT images of tumor oxygen metabolism have not been achieved due to lack of information about blood flow. In the future, DOT plus blood-flow information (derived either by optical means[92,93] or by another technique) hold potential for imaging of tumor metabolism.

The cysts in our DOT images (not shown) exhibited low rTHC, $r\mu_s'$, and StO_2. This observation is in stark contrast to the high rTHC, and $r\mu_s'$ of the invasive carcinomas. Generally, cysts have been associated with low scattering in DOT images by other groups,[24,68,69] because the fluid they enclose is optically thin. Sometimes cysts have exhibited lower THC and StO_2 compared to normal tissue as well.[26]

The fibroadenoma in our DOT images showed little or no contrast, as was the case for the lobular carcinoma *in situ*. Other groups have reported difficulty detecting fibroadenomas.[69] In our analysis, we included lobular carcinoma *in situ* in the benign category to be consistent with such recognition in the clinic.[94,95]

4.5 Core Biopsy Effects

It has been speculated that core biopsy can cause bleeding significant enough to interfere with the hemoglobin-based DOT signal. In some cases, where the bleeding was severe enough to be detected by eye, the corresponding bruise region in the DOT images showed lower blood-oxygen levels compared to the surrounding tissue as well as elevated THC and

scattering. Lower StO_2 in this case may be due to a lack of oxygen supply to the noncirculating blood that has permeated into the extracellular space. However, when these parameters were averaged over the population of each group (i.e., malignant group before and after core biopsy), differences between the pre- and postbiopsy groups were not apparent. This observation indicates that overall variation within each malignant group is more than the variation due to core-biopsy effect. In addition, no correlation between the tumor-to-normal ratios of optical parameters and the number of days after biopsy was found (data not shown). This result could change for DOT data measured less than 1 week after the core biopsy. Clearly, in order to fully understand the effect of core biopsy or fine needle aspiration on the DOT signal, it is desirable to perform a longitudinal study following subjects before and after core biopsy (which is beyond the scope of the present publication).

4.6 Selection of Optimal Parameters to Differentiate Benign and Malignant Lesions

In order to assess which optical parameters among many are useful for differentiating benign and malignant tumors, we employed an ROC curve analysis for each parameter. Because the influence of core biopsy on our DOT data was determined to be negligible (see Sec. 3.3), we combined the two groups into one malignant cancer category and compared the malignant group ($N=41$) with the benign group ($N=10$). The AUC of rTHC, $r\mu_s'$, rHbO$_2$, and OI suggested good discriminatory power (<0.90) to differentiate malignant and benign groups.

ROC curve analysis is important for testing the effectiveness of any diagnostic imaging method. So far, only a few diffuse optics groups have attempted ROC curve analysis. Chance et al.[25] used a combination of relative THC and StO_2 (derived by DOS) of tumors measured with respect to the contralateral side and obtained 95% AUC to discern cancer from normal tissue. In our case, rStO$_2$ did not have much discriminatory power. Furthermore, due to our small number of benign cases, any attempt to combine multiple parameters would result in an overfit of the statistical model. Poplack et al.[41] achieved 88% AUC for differentiating cancer from normal tissue and 76% AUC for differentiating malignant cancer from benign lesion distinction using rTHC derived from 3-D DOT images for a subset of subjects with lesions larger than 6 mm; their AUC decreased when smaller lesions were included in the data set. However, these findings do not represent a final assessment of DOT performance. Each of these papers focused on demonstrations of particular methodology and were not representative of all or even optimized diffuse optical methods. The discrepancy among groups could be a function of methods (e.g., two parameters versus one parameter, localization of tumor with other modalities, etc.) and the variations in the subject groups (e.g., lesion size, percentage of benign and malignant lesions).

4.7 Future Study Design

A key limitation in our study, as well as those published by other groups, is a small sample size, especially of benign lesions. The lack of statistical significance in benign tumors arises from two effects: (i) a lack of intrinsic lesion-to-normal contrast in some benign lesions, and (ii) the small sample size. By averaging over different types of benign lesions, distinct

optical signatures of certain lesion types (e.g., cysts) have not been isolated. For future studies, it will be necessary to collect more data (especially benign cases) in order to build a stronger predictive model to differentiate benign and malignant lesions. Also, with more data, it should be possible to find the best combination of multiple parameters for differentiation of malignant and benign lesions, and further differentiation of lesion types (e.g., ductal carcinoma *in situ* versus invasive ductal carcinoma, and fibroadenoma versus cyst). Furthermore, in the future we can use a large population of lesions without regional averaging (i.e., including the intraregion variability of individual subjects) to develop more advanced analyses that differentiate lesion types and automatically locate lesions in the reconstructed images.

The current instrumentation and analysis scheme is limited because only four lasers were frequency modulated and because this group did not include the 905 nm laser. Thus, it was difficult to directly measure bulk water content. For this reason, we assumed background water and lipid concentrations to be 31 and 57%, respectively, following previous reports in the literature.[56–58] As per continuous-wave diffuse optical tomography, we chose not to reconstruct water concentration, because approximately half of the patient data was taken without the 905 nm source. Of course, fixing the water concentration can introduce errors in our estimation of Hb and HbO_2 concentration. To explore the effects of assumed background water concentration on the relative tumor-to-normal ratios, we performed a full reconstruction on selected data set ($N=4$) with different assumed water concentrations (i.e., at 15, 31, 45, and 60%). These variations in water concentration did not change the overall spatial features of the image (e.g., regions with contrast remained the same). However, extracted rTHC, rStO$_2$, $r\mu_s'$, rHb, rHbO$_2$, and OI did vary somewhat, differing by 4–7, 3–6, 5–7, 7–10, 6–7, and 6–14%, respectively, from results with 31% water concentration. These variations are less than intersubject variability (95% CI) shown in Table 4.

We will address these hardware limitations with "next generation" DOT instrument.[96] This instrument will employ light sources at optimal wavelengths, will add water sensitive wavelengths, and will carry out all measurements in the frequency domain. This approach will therefore reduce absorption-scattering crosstalk and will permit reconstruction of water and lipid concentrations. Finally, such new instrumentation should more readily permit separation of the scattering prefactor A from the scattering power b. In addition, more light-source positions will permit denser sampling of small breasts. We will use a sophisticated, automated deformation algorithm[97] to coregister MRI and DOT images taken nonconcurrently. Furthermore, the new system will operate in any of sagittal, craniocaudal, or mediolateral oblique compression, allowing us to better match the clinical imaging geometry and improve our nonconcurrent coregistration. The reconstruction algorithm will be improved to further reduce image artifacts and to employ MRI-derived anatomical information to constrain our DOT reconstruction algorithms.

5 Conclusion

In this paper, we reported diffuse optical tumor-to-normal contrast extracted from 3-D reconstructions of 51 breast tu-
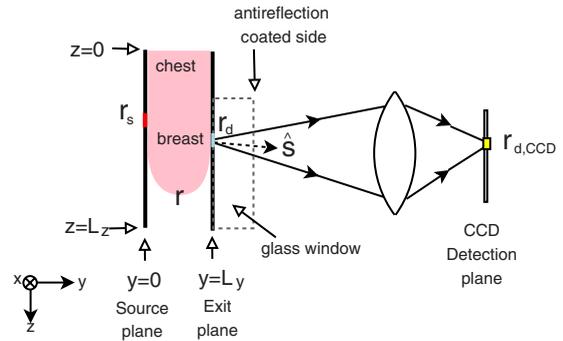

Fig. 7 Schematic of breast DOT instrument.

mors using our parallel-plate DOT system. Elevated regions of THC and scattering in malignant cancers in DOT images generally correlated well with tumor regions identified by MRI. By contrast, cysts exhibited lower scattering than the surrounding tissue, and fibroadenomas showed zero or relatively weaker contrast in THC and scattering. The tumor-to-normal ratios in THC, HbO_2, scattering, and the OI of the malignant cancer group were statistically significant and different from unity, whereas those of the benign tumor group were not. These parameters also exhibited high AUC values for distinguishing between malignant and benign lesions. The effect of core biopsy in our malignant tumor group was not statistically significant when DOT measurement was done more than 1 week after core biopsy. Our results suggest that benign and malignant lesions can be distinguished by quantitative 3-D DOT. This distinction between benign and malignant lesions is important for efforts to increase sensitivity and specificity of overall breast cancer diagnosis and for establishing the reliability of the technology for breast cancer therapy monitoring applications.

Appendix

In this section we review the relationship between the measured signal at the CCD and the photon fluence rate at the exit plane of the sample. We also briefly describe the formulation of the objective function used for the inverse problem, including regularization.

Relationship between the fluence rate and the signal detected at the CCD

Consider the schematic of the measurement geometry shown in Fig. 7. A CCD image is obtained for each source position

and wavelength. Let $\Phi(\lambda_\omega, \mathbf{r}_s, \mathbf{r})$ denote the fluence rate due to source light originating at $\mathbf{r}_s$ with wavelength λ_ω. The variable $\mathbf{r}$ denotes position in the sample, including at the exit plane. Furthermore, let $\mathbf{J}(\lambda_\omega, \mathbf{r}_s, \mathbf{r})$ denote the corresponding photon flux at $\mathbf{r}$ and $L(\lambda_\omega, \mathbf{r}_s, \mathbf{r}, \hat{s})$ denote the corresponding photon radiance $\mathbf{r}$ traveling in the $\hat{s}$ direction. In the P_1 approximation of the transport equation[98,99] (i.e., the diffusion approximation),

$$L(\lambda_\omega, \mathbf{r}_s, \mathbf{r}, \hat{s}) = (1/4\pi)\Phi(\lambda_\omega, \mathbf{r}_s, \mathbf{r}) + (3/4\pi)\mathbf{J}(\lambda_\omega, \mathbf{r}_s, \mathbf{r}) \cdot \hat{s}.$$

The signal at the CCD plane is detected at a set of discrete points (pixels) of finite size. We denote the detection position on the CCD as $\mathbf{r}_{d,CCD}$. The power, P, reaching one of the CCD pixels centered at position $\mathbf{r}_{d,CCD}$ is explicitly related to $L(\lambda_\omega, \mathbf{r}_s, \mathbf{r}, \hat{s})$, i.e.,

$$P(\lambda_\omega, \mathbf{r}_s, \mathbf{r}_{d,CCD}) =$$
$$\underset{\text{exit plane}}{\iint} d^2\mathbf{r} \underset{\text{solid angle}}{\int} d\Omega(\hat{s}) L(\lambda_\omega, \mathbf{r}_s, \mathbf{r}, \hat{s}) T_F(\hat{s}) R(\mathbf{r}, \mathbf{r}_{d,CCD}, \hat{s}).$$

$$(1)$$

The angular integral extends over the whole half-space solid angle, and the spatial integral extends over the entire exit plane. Here, $T_F(\hat{s})$ is a Fresnel transmission factor at the boundary, assumed independent of $\mathbf{r}$ at the exit plane and $\mathbf{r}_{d,CCD}$; it accounts for the relative transmission of light emitted from the same point along different directions into the detection system. $R(\mathbf{r}, \mathbf{r}_{d,CCD}, \hat{s})$ is a response function which gives the probability that light emitted from position $\mathbf{r}$ in the $\hat{s}$ direction landed in the pixel centered at $\mathbf{r}_{d,CCD}$. We further assume that for each $\mathbf{r}_{d,CCD}$ this response function is sharply peaked at $\mathbf{r} = \mathbf{r}_d$, i.e., the response function has a sharp maximum (less than unity) for a small patch of area $\mathcal{A}$ centered on $\mathbf{r}_d$ in the exit plane, and for $\hat{s}$ within the numerical aperture of the detection system. The response function is zero otherwise. Typically, $\mathcal{A}$ will be on the order of 0.1 to 1 mm^2, much larger than the CCD pixel area due to the lens demagnification. The maximum value of this response function also decreases as the radial distance (distance between $\mathbf{r}_d$ and the lens axis) increases due to beam vignetting.[100]

To evaluate Eq. (1), we use Fick's law to relate photon fluence rate to photon flux, i.e., $\mathbf{J}(\mathbf{r}) = -(D/v)\nabla\Phi(\mathbf{r})$, and we apply the partial current boundary condition for the radiance at the exit plane, i.e., $\Phi(\mathbf{r}) = (1 + R_{\text{eff}}/1 - R_{\text{eff}})2(D/v) \times (\partial\Phi/\partial y)$.[101] Here, D is the the photon diffusion coefficient $(D \cong v/3\mu_s')$, μ_s' is the reduced scattering coefficient, v is the velocity of light in the medium, and R_{eff} is the effective reflectance at boundary. Evaluating Eq. (1) gives

$$P(\lambda_\omega, \mathbf{r}_s, \mathbf{r}_{d,CCD}) \cong \Phi_m(\lambda_\omega, \mathbf{r}_s, \mathbf{r}_d)\mathcal{A}G(\mathbf{r}_d) \quad (2)$$

Here, we have assumed that the measured fluence rate, Φ_m, is roughly constant over the patch area $\mathcal{A}$, and we have associated a single $\mathbf{r}_d$ at the exit plane with each $\mathbf{r}_{d,CCD}$. $G(\mathbf{r})$ is a geometric factor that includes the Fresnel factor integral over the system numerical aperture and the Vignetting effect. The corresponding CCD readout is $N(\lambda_\omega, \mathbf{r}_s, \mathbf{r}_{d,CCD}) = \Phi_m(\lambda_\omega, \mathbf{r}_s, \mathbf{r}_d)\mathcal{A}G(\mathbf{r}_d)v(\lambda_\omega)g\Delta t$, where $v(\lambda_\omega)$ is the quan-

tum efficiency of the detector, Δt is the camera exposure time, and g accounts for internal amplifier gains in the detection device. Thus, $N(\lambda_\omega, \mathbf{r}_s, \mathbf{r}_{d,CCD})$ is proportional to $\Phi_m(\lambda_\omega, \mathbf{r}_s, \mathbf{r}_d)$.

In order to extract tissue optical properties we must compare $\Phi_m(\lambda_\omega, \mathbf{r}_s, \mathbf{r}_d)$ to the calculated fluence rate at the exit plane $\Phi_c(\lambda_\omega, \mathbf{r}_s, \mathbf{r}_d)$ based on the optical property distribution in the sample. We compute $\Phi_c(\lambda_\omega, \mathbf{r}_s, \mathbf{r}_d)$ using a finite-element-method-based numerical solver[59] wherein we employ a nonuniform unstructured mesh with higher nodal concentrations at source/detector planes in order to increase the forward model accuracy and suppress image artifacts associated with sources and detectors.[60] We model our reconstruction volume to mimic the physical boundary system of the breast box and also the breast and Intralipid interfaces. The effective reflectance coefficient, R_{eff}, at the boundary is estimated based on the ratio between the refractive index of the sample medium (n) and the outside medium (n_{out}).[102] At $y = L_y$, we have a glass window (with antireflection coating on the opposite side of the exit plane) which we model as a tissue–glass interface (i.e., $n = 1.4$ and $n_{\text{out}} = 1.5$). The $z = 0$ boundary is modeled as a tissue–air boundary (i.e., $n = 1.4$ and $n_{\text{out}} = 1.0$). The rest of the black-coated boundaries are modeled as having total absorption $(R_{\text{eff}} = 0)$. Note that our reconstruction volume in the z direction extends upward to account for the presence of the chest.

Objective Function

The objective function, χ^2, is a measure of the difference between Φ_m and Φ_c, summed over all the measurements. In our case, we modify a Rytov-type objective function for the multispectral method by summing over all source–detector position pairs and all wavelengths. The detailed form of χ^2 is as follows:

$$\chi^2 = \frac{1}{2}\sum_{w=1}^{N_\lambda}\sum_{s=1}^{N_s}\sum_{d=1}^{N_d}\left\{\ln\left[\frac{\Phi_m(\lambda_w, \mathbf{r}_s, \mathbf{r}_d)}{\Phi_m^R(\lambda_w, \mathbf{r}_s, \mathbf{r}_d)}\frac{\Phi_c^R(\lambda_w, \mathbf{r}_s, \mathbf{r}_d)}{\Phi_c(\lambda_w, \mathbf{r}_s, \mathbf{r}_d)}\right]\right\}^2 + Q,$$

$$(3)$$

$$= \frac{1}{2}\sum_{w=1}^{N_\lambda}\sum_{s=1}^{N_s}\sum_{d=1}^{N_d}\left\{\ln\left[\frac{N(\lambda_w, \mathbf{r}_s, \mathbf{r}_d)}{N^R(\lambda_w, \mathbf{r}_s, \mathbf{r}_d)}\frac{\Phi_c^R(\lambda_w, \mathbf{r}_s, \mathbf{r}_d)}{\Phi_c(\lambda_w, \mathbf{r}_s, \mathbf{r}_d)}\right]\right\}^2 + Q.$$

$$(4)$$

Here, the image norm $Q = \sum_{k=1}^{N_t}\gamma(\mathbf{r}_k)\|\mu(\mathbf{r}_k) - \mu^0(\mathbf{r}_k)\|^2$, where N_t is the total number of voxels. μ stands for solution vector (i.e., μ_a and D) and the superscript 0 refers to the value of $\mu(\mathbf{r}_k)$ in the previous iteration. In the multispectral approach, μ are computed based on the chromophore concentrations, C_l, via the relation $\mu_a(\lambda) = \sum_{l=1}^L \epsilon_l(\lambda)C_l + \mu_a^{\text{bg}}(\lambda)$; the scattering factors A and b are related via the relation $\mu_s'(\lambda) = A\lambda^{-b}$. N_λ, N_s, and N_d are the number of wavelengths, sources and detectors, respectively. The superscript R refers to quantities (i.e., Φ_m, Φ_c, or N) derived from the homogeneous Intralipid/Ink reference sample. We were able to use our CCD readings, N and N^R, directly in place of Φ_m and Φ_m^R, because the proportionality constants are assumed identical between the breast and Intralipid/Ink measurements (i.e., the constants

cancel one another). The normalization with the Intralipid/Ink measurement is important for the integrity of our reconstruction, because it minimizes systematic errors that may be present in our measurement, including the lens Vignetting effect, and source strength fluctuations among different source positions, etc.

$\gamma(\mathbf{r}_k)$ is a spatially variant regularization factor

$$\gamma(\mathbf{r}_k) = \alpha \left\{ \exp\left[-\left(\frac{x - x_{\min}}{L_x}\right)^2 \right] + \exp\left[-\left(\frac{x - x_{\max}}{L_x}\right)^2 \right] \right.$$
$$+ \exp\left[-\left(\frac{y - y_{\min}}{L_y/2}\right)^2 \right] + \exp\left[-\left(\frac{y - y_{\max}}{L_y/2}\right)^2 \right]$$
$$\left. + \exp\left[-\left(\frac{z - z_{\min}}{L_z}\right)^2 \right] + \exp\left[-\left(\frac{z - z_{\max}}{L_z}\right)^2 \right] \right\}.$$
$$(5)$$

Here, α is the regularization parameter and L_x, L_y, L_z are the dimensions of the sample box. $x_{\min}, y_{\min}, z_{\min}$ and $x_{\max}, y_{\max}, z_{\max}$ are minimum and maximum coordinates of the sample box, respectively. y is the axis perpendicular to the source and detection planes. For L-curve analysis, we varied α as described in the text (Section 2.3). We use the nonlinear conjugate gradient method to minimize χ^2, computing the search direction based on the gradient of χ^2.[61] This method does not require a matrix inversion for computing search directions. Therefore, it is especially useful for systems with a large number of source–detector pairs and large reconstruction domains wherein building and inverting the Jacobian matrix can be computationally difficult and even impossible due to memory limitations.

References

1. L. A. G. Ries, D. Melbert, M. Krapcho, D. G. Stinchcomb, N. Howlander, M. J. Horner, A. Mariotto, B. A. Miller, E. J. Feuer, S. F. Altekruse, D. R. Lewis, L. Clegg, M. P. Eisner, M. Reichmann, and B. K. Edwards (eds.), "SEER cancer statistics review, 1975–2005," National Cancer Institute, Bethesda, MD, http://seer.cancer.gov/csr/1975_2005/, based on 2007 SEER data submission (2008).
2. K. Kerlikowske, J. Barclay, D. Grady, E. A. Sickles, and V. Ernster, "Comparison of risk factors for ductal carcinoma *in situ* and invasive breast cancer," *J. Natl. Cancer Inst. (1940-1978)* **89**(1), 76–82 (1997).
3. I. G. Murphy, M. F. Dillon, A. O'Doherty, E. W. McDermott, G. Kelly, N. O'Higgins, and A. D. K. Hill, "Analysis of patients with false negative mammography and symptomatic breast carcinoma," *J. Surg. Oncol.* **96**, 457–463 (2007).
4. S. W. Fletcher, "Breast cancer screening among women in their forties: An overview of the issues," *J. Natl. Cancer Inst. Monogr.* **22**, 15–18 (1997).
5. J. G. Elmore, M. B. Barton, V. M. Moceri, S. Polk, P. J. Arena, and S. W. Fletcher, "Ten-year risk of false positive screening mammograms and clinical breast examinations," *N. Engl. J. Med.* **338**, 1089–1096 (1998).
6. S. K. Goergen, J. Evans, G. P. B. Cohen, and J. H. MacMillan, "Characteristics of breast carcinomas missed by screening radiologists," *Radiology* **204**, 131–135 (1997).
7. R. L. Birdwell, D. M. Ikeda, K. F. O'Shaughnessy, and E. A. Sickles, "Mammographic characteristics of 115 missed cancers later detected with screening mammography and the potential utility of computer-aided detection," *Radiology* **219**(1), 192–202 (2001).
8. J. Wang, T. T. Shih, J. C. Hsu, and Y. W. Li, "The evaluation of false negative mammography from malignant and benign breast lesions," *J. Clin. Imaging* **24**, 96–103 (2000).
9. M. A. Franceschini, K. T. Moesta, S. Fantini, G. Gaida, E. Gratton, H. Jess, W. W. Mantulin, M. Seeber, P. M. Schlag, and M. Kaschke, "Frequency-domain techniques enhance optical mammography: Initial clinical results," *Proc. Natl. Acad. Sci. U.S.A.* **94**, 6468–6473 (1997).
10. S. B. Colak, M. B. van der Mark, G. W. Hooft, J. H. Hoogenraad, E. S. van der Linden, and F. A. Kuijpers, "Clinical optical tomography and NIR spectroscopy for breast cancer detection," *IEEE J. Quantum Electron.* **5**(4), 1143–1158 (1999).
11. V. Ntziachristos, A. G. Yodh, M. Schnall, and B. Chance, "Concurrent MRI and diffuse optical tomography of breast after indocyanine green enhancement," *Proc. Natl. Acad. Sci. U.S.A.* **97**, 2767–2772 (2000).
12. B. J. Tromberg, N. Shah, R. Lanning, A. Cerussi, J. Espinoza, T. Pham, L. Svaasand, and J. Butler, "Non-invasive *in vivo* characterization of breast tumors using photon migration spectroscopy," *Neoplasia* **2**, 26–40 (2000).
13. B. W. Pogue, S. P. Poplack, T. O. McBride, W. A. Wells, K. S. Osterman, U. L. Osterberg, and K. D. Paulsen, "Quantitative hemoglobin tomography with diffuse near-infrared spectroscopy: Pilot results in the breast," *Radiology* **218**, 261–266 (2001).
14. H. Jiang, Y. Xu, N. Ifitimia, J. Eggert, K. Klove, L. Baron, and L. Fajardo, "Three-dimensional optical tomographic imaging of breast in a human subject," *IEEE Trans. Med. Imaging* **20**, 1334–1340 (2001).
15. H. Dehghani, B. W. Pogue, S. D. Jiang, B. Brooksby, and K. D. Paulsen, "Three-dimensional optical tomography: Resolution in small-object imaging," *Appl. Opt.* **42**, 3117–3128 (2003).
16. A. Li, E. L. Miller, M. E. Kilmer, T. J. Brukilacchio, T. Chaves, J. Stott, Q. Zhang, T. Wu, M. Chorlton, R. H. Moore, D. B. Kopans, and D. A. Boas, "Tomographic optical breast imaging guided by three-dimensional mammography," *Appl. Opt.* **42**, 5181–5190 (2003).
17. Q. I. Zhu, M. M. Huang, N. G. Chen, K. Zarfos, B. Jagjivan, M. Kane, P. Hedge, and S. H. Kurtzman, "Ultrasound-guided optical tomographic imaging of malignant and benign breast lesions: Initial clinical results of 19 cases," *Neoplasia* **5**, 379–388 (2003).
18. D. B. Jakubowski, A. E. Cerussi, F. Bevilacqua, N. Shah, D. Hsiang, J. Butler, and B. J. Tromberg, "Monitoring neoadjuvant chemotherapy in breast cancer using quantitative diffuse optical spectroscopy: A case study," *J. Biomed. Opt.* **9**, 230–238 (2004).
19. R. Choe, A. Corlu, K. Lee, T. Durduran, S. D. Konecky, M. Grosicka-Koptyra, S. R. Arridge, B. J. Czerniecki, D. L. Fraker, A. DeMichele, B. Chance, M. A. Rosen, and A. G. Yodh, "Diffuse optical tomography of breast cancer during neoadjuvant chemotherapy: A case study with comparison to MRI," *Med. Phys.* **32**(4), 1128–1139 (2005).
20. C. H. Schmitz, D. P. Klemer, R. Hardin, M. S. Katz, Y. Pei, H. L. Graber, M. B. Levin, R. D. Levina, N. A. Fraco, W. B. Solomon, and R. L. Barbour, "Design and implementation of dynamic near-infrared optical tomographic imaging instrumentation for simultaneous dual-breast measurements," *Appl. Opt.* **44**, 2140–2153 (2005).
21. X. Intes, S. Djeziri, Z. Ichalalene, N. Mincu, Y. Wang, P. St-Jean, F. Lesage, D. Hall, D. Boas, M. Polyzos, D. Fleiszer, and B. Mesurolle, "Time-domain optical mammography SoftScan: Initial results," *Acad. Radiol.* **12**, 934–947 (2005).
22. D. Grosenick, K. T. Moesta, M. Möller, J. Mucke, H. Wabnitz, B. Gebauer, C. Stroszczynski, B. Wassermann, P. M. Schlag, and H. Rinneberg, "Time-domain scanning optical mammography: I. Recording and assessment of mammograms of 154 patients," *Phys. Med. Biol.* **50**(11), 2429–2450 (2005).
23. D. Grosenick, H. Wabnitz, K. T. Moesta, J. Mucke, P. M. Schlag, and H. Rinneberg, "Time-domain scanning optical mammography: II. Optical properties and tissue parameters of 87 carcinomas," *Phys. Med. Biol.* **50**(11), 2451–2468 (2005).
24. L. Spinelli, A. Torricelli, A. Pifferi, P. Taroni, G. Danesini, and R. Cubeddu, "Characterization of female breast lesions from multi-wavelength time-resolved optical mammography," *Phys. Med. Biol.* **50**(11), 2489–2502 (2005).
25. B. Chance, S. Nioka, J. Zhang, E. F. Conant, E. Hwang, S. Briest, S. G. Orel, M. D. Schnall, and B. J. Czerniecki, "Breast cancer detection based on incremental biochemical and physiological properties of breast cancers: A six-year, two-site study," *Acad. Radiol.* **12**, 925–933 (2005).
26. L. C. Enfield, A. P. Gibson, N. L. Everdell, D. T. Delpy, M. Schweiger, S. R. Arridge, C. Richardson, M. Keshtgar, M. Douek, and J. C. Hebden, "Three-dimensional time-resolved optical mammography of the uncompressed breast," *Appl. Opt.* **46**, 3628–3638 (2007).

27. Q. Zhu, S. H. Kurtzma, P. Hegde, S. Tannenbaum, M. Kane, M. Huang, N. G. Chen, B. Jagjivan, and K. Zarfos, "Utilizing optical tomography with ultrasound localization to image heterogeneous hemoglobin distribution in large breast cancers," *Neoplasia* **7**(3), 263–270 (2005).

28. S. Srinivasan, B. W. Pogue, B. Brooksby, S. Jiang, H. Dehghani, C. Kogel, W. A. Wells, S. P. Poplack, and K. D. Paulsen, "Near-Infrared characterization of breast tumors *in vivo* using spectrally-constrained reconstruction," *Technol. Cancer Res. Treat.* **4**, 513–526 (2005).

29. C. Li, S. R. Grobmyer, N. Massol, L. X, Q. Zhang, L. Chen, L. L. Fajardo, and H. Jiang, "Noninvasive *in vivo* tomographic optical imaging of cellular morphology in the breast: Possible convergence of microscopic pathology and macroscopic radiology," *Med. Phys.* **35**, 2493–2501 (2008).

30. J. Folkman, K. Watson, D. Ingber, and D. Hanahan, "Induction of angiogenesis during the transition from hyperplasia to neoplasia," *Nature (London)* **339**, 58–61 (1989).

31. P. Vaupel, O. Thews, D. K. Kelleher, and M. Hoeckel, "Current status of knowledge and critical issues in tumor oxygenation: Results from 25 years research in tumor pathophysiology," *Adv. Exp. Med. Biol.* **454**, 591–602 (1998).

32. P. Vaupel, K. Schlenger, C. Knoop, and M. Hockel, "Oxygenation of human tumors: evaluation of tissue oxygen distribution in breast cancers by computerized O_2 tension measurements," *Cancer Res.* **51**(12), 3316–22 (1991).

33. N. Weidner, J. Folkman, F. Pozza, P. Bevilacqua, D. C. Allred, D. H. Moore, S. Meli, and G. Gasparini, "Tumor angiogenesis: A new significant and independent prognostic indicator in early-stage breast carcinoma," *J. Natl. Cancer Inst. (1940-1978)* **84**, 1875–1887 (1992).

34. S. Thomsen and D. Tatman, "Physiological and pathological factors of human breast disease that can influence optical diagnosis," *Ann. N.Y. Acad. Sci.* **838**, 171–193 (1998).

35. J. R. Mourant, J. P. Freyer, A. H. Hielscher, A. A. Eick, D. Shen, and T. M. Johnson, "Mechanisms of light scattering from biological cells relevant to noninvasive optical-tissue diagnosis," *Appl. Opt.* **37**, 3586–3593 (1998).

36. J. C. Hebden, T. D. Yates, A. Gibson, N. Everdell, S. R. Arridge, D. W. Chicken, M. Douek, and M. R. S. Keshtgar, "Monitoring recovery after laser surgery of the breast with optical tomography: A case study," *Appl. Opt.* **44**(10), 1898–1904 (2005).

37. N. Shah, J. Gibbs, D. Wolverton, A. Cerussi, N. Hylton, and B. J. Tromberg, "Combined diffuse optical spectroscopy and contrast-enhanced magnetic resonance imaging for monitoring breast cancer neoadjuvant chemotherapy: A case study," *J. Biomed. Opt.* **10**, 051503 (2005).

38. A. Cerussi, D. Hsiang, N. Shah, R. Mehta, A. Durkin, J. Butler, and B. J. Tromberg, "Predicting response to breast cancer neoadjuvant chemotherapy using diffuse optical spectroscopy," *Proc. Natl. Acad. Sci. U.S.A.* **104**, 4014–4019 (2007).

39. Q. Zhu, S. Tannenbaum, P. Hegde, M. Kane, C. Xu, and S. H. Kurtzman, "Noninvasive monitoring of breast cancer during neoadjuvant chemotherapy using optical tomography with ultrasound localization," *Neoplasia* **10**, 1028–1040 (2008).

40. A. Cerussi, N. Shah, D. Hsiang, A. Durkin, J. Butler, and B. J. Tromberg, "*In vivo* absorption, scattering, and physiologic properties of 58 malignant breast tumors determined by broadband diffuse optical spectroscopy," *J. Biomed. Opt.* **11**, 044005 (2006).

41. S. P. Poplack, T. D. Tosteson, W. A. Wells, B. W. Pogue, P. M. Meaney, A. Hartov, C. A. Kogel, S. K. Soho, J. J. Gibson, and K. D. Paulsen, "Electromagnetic breast imaging: Results of a pilot study in women with abnormal mammograms," *Radiology* **243**(2), 350–359 (2007).

42. D. R. Leff, O. J. Warren, L. C. Enfield, A. Gibson, T. Athanasiou, D. K. Patten, J. Hebden, G. Z. Yang, and A. Darzi, "Diffuse optical imaging of the healthy and diseased breast: A systematic review," *Breast Cancer Res. Treat.* **108**, 9–22 (2008).

43. S. D. Konecky, G. Y. Panasyuk, K. Lee, V. A. Markel, A. G. Yodh, and J. C. Schotland, "Imaging complex structures with diffuse light," *Opt. Express* **16**, 5048–5060 (2008).

44. J. P. Culver, R. Choe, M. J. Holboke, L. Zubkov, T. Durduran, A. Slemp, V. Ntziachristos, B. Chance, and A. G. Yodh, "Three-dimensional diffuse optical tomography in the parallel plane transmission geometry: Evaluation of a hybrid frequency domain/continuous wave clinical system for breast imaging," *Med. Phys.* **30**, 235–247 (2003).

45. A. Corlu, T. Durduran, R. Choe, M. Schweiger, E. M. C. Hillman, S. R. Arridge, and A. G. Yodh, "Uniqueness and wavelength optimization in continuous-wave multispectral diffuse optical tomography," *Opt. Lett.* **28**, 2339–2341 (2003).

46. A. Corlu, R. Choe, T. Durduran, K. Lee, M. Schweiger, S. R. Arridge, E. M. C. Hillman, and A. G. Yodh, "Diffuse optical tomography with spectral constraints and wavelength optimization," *Appl. Opt.* **44**(11), 2082–2093 (2005).

47. Y. S. Yang, H. L. Liu, X. D. Li, and B. Chance, "Low-cost frequency-domain photon migration instrument for tissue spectroscopy, oximetry, and imaging," *Opt. Eng.* **36**(5), 1562–1569 (1997).

48. T. Yates, J. C. Hebden, A. Gibson, N. Everdell, S. R. Arridge, and M. Douek, "Optical tomography of the breast using a multi-channel time-resolved imager," *Phys. Med. Biol.* **50**(11), 2503–2518 (2005).

49. S. Prahl, "Optical Properties Spectra," ⟨http://omlc.ogi.edu/spectra/index.html⟩ (2007).

50. A. Ishimaru, *Wave Propagation and Scattering in Random Media*, Academic Press, San Diego (1978).

51. K. Furutsu, "On the diffusion equation derived from the space-time transport equation," *J. Opt. Soc. Am. A* **70**, 360–366 (1980).

52. R. A. J. Groenhuis, H. A. Ferwerda, and J. J. Ten Bosch, "Scattering and absorption of turbid materials determined from reflection measurements. I. Theory." *Appl. Opt.* **22**, 2456–2462 (1983).

53. J. R. Mourant, T. Fuselier, J. Boyer, T. M. Johnson, and I. J. Bigio, "Predictions and measurements of scattering and absorption over broad wavelength ranges in tissue phantoms," *Appl. Opt.* **39**, 949–957 (1997).

54. F. Bevilacqua, A. J. Berger, A. E. Cerussi, D. Jakubowski, and B. J. Tromberg, "Broadband absorption spectroscopy in turbid media by combined frequency-domain and steady-state methods," *Appl. Opt.* **39**, 6498–6507 (2000).

55. T. Durduran, R. Choe, J. P. Culver, L. Zubkov, M. J. Holboke, J. Giammarco, B. Chance, and A. G. Yodh, "Bulk optical properties of healthy female breast tissue," *Phys. Med. Biol.* **47**, 2847–2861 (2002).

56. H. Q. Woodard and D. R. White, "The composition of body tissues," *Br. J. Radiol.* **59**, 1209–1219 (1986).

57. D. R. White, H. Q. Woodard, and S. M. Hammond, "Average soft-tissue and bone models for use in radiation dosimetry," *Br. J. Radiol.* **60**, 907–913 (1987).

58. N. A. Lee, H. Rusinek, J. C. Weinreb, R. Chandra, R. C. Singer, and G. M. Newstead, "Fatty and fibroglandular tissue volumes in the breasts of women 20–83 years old: Comparison of X-ray mammography and computer-assisted MR imaging," *AJNR Am. J. Neuroradiol.* **168**, 501–506 (1997).

59. S. R. Arridge and M. Schweiger, "Photon-measurement density functions. Part 2: Finite-element-method calculations," *Appl. Opt.* **34**(34), 8026–8036 (1995).

60. K. Lee, R. Choe, A. Corlu, S. D. Konecky, T. Durduran, and A. G. Yodh, "Artifact reduction in CW transmission diffuse optical tomography," in *Biomedical Topical Meetings on CD-ROM*, WB2, The Optical Society of America, Washington DC (2004).

61. S. R. Arridge and M. Schweiger, "A gradient-based optimisation scheme for optical tomography," *Opt. Express* **2**(6), 213–226 (1998).

62. B. W. Pogue, T. O. McBride, J. Prewitt, U. L. Osterberg, and K. D. Paulsen, "Spatially variant regularization improves diffuse optical tomography," *Appl. Opt.* **38**, 2950–2961 (1999).

63. L. Kaufman and A. Neumaier, "PET regularization by envelope guided conjugate gradients," *IEEE Trans. Med. Imaging* **15**, 385–389 (1996).

64. A. Corlu, R. Choe, T. Durduran, K. Lee, S. D. Konecky, and A. G. Yodh, "Regularization of diffuse optical tomography images by envelope guided conjugate gradients," in *Biomedical Topical Meetings on CD-ROM*, ThD4, The Optical Society of America, Washington DC (2004).

65. R Development Core Team, *R: A Language and Environment for Statistical Computing*, R Foundation for Statistical Computing, Vienna, Austria (2007).

66. J. C. Pinheiro and D. M. Bates, *Mixed-Effects Models in S and S-PLUS*, Springer, New York (2000).

67. T. Sing, O. Sander, N. Beerenwinkel, and T. Lengauer, "ROCR: visualizing classifier performance in R," *Bioinformatics* **21**, 3940–3941 (2005).

68. X. J. Gu, Q. Z. Zhang, M. Bartlett, L. Schutz, L. L. Fajardo, and H. B. Jiang, "Differentiation of cysts from solid tumors in the breast

with diffuse optical tomography," *Acad. Radiol.* **11**, 53–60 (2004).

69. P. Taroni, A. Torricelli, L. Spinelli, A. Pifferi, F. Arpaia, G. Danesini, and R. Cubeddu, "Time-resolved optical mammography between 637 and 985 nm: Clinical study on the detection and identification of breast lesions," *Phys. Med. Biol.* **50**(11), 2469–2488 (2005).

70. V. Ntziachristos, A. G. Yodh, M. D. Schnall, and B. Chance, "MRI-guided diffuse optical spectroscopy of malignant and benign breast lesions," *Neoplasia* **4**, 347–354 (2002).

71. B. Brooksby, B. W. Pogue, S. Jiang, H. Dehghani, S. Srinivasan, C. Kogel, T. D. Tosteson, J. Weaver, S. P. Poplack, and K. D. Paulsen, "Imaging breast adipose and fibroglandular tissue molecular signatures by using hybrid MRI-guided near-infrared spectral tomography," *Proc. Natl. Acad. Sci. U.S.A.* **103**, 8828–8833 (2006).

72. C. M. Carpenter, B. W. Pogue, S. Jiang, H. Dehghani, X. Wang, K. D. Paulsen, W. A. Wells, J. Forero, C. Kogel, J. B. Weaver, S. P. Poplack, and P. A. Kaufman, "Image-guided optical spectroscopy provides molecular-specific information *in vivo*: MRI-guided spectroscopy of breast cancer hemoglobin, water, and scatterer size," *Opt. Lett.* **32**(8), 933–935 (2007).

73. Q. Zhang, T. J. Brukilacchio, A. Li, J. J. Stott, T. Chaves, E. Hillman, T. Wu, A. Chorlton, E. Rafferty, R. H. Moore, D. B. Kopans, and D. A. Boas, "Coregistered tomographic X-ray and optical breast imaging: Initial results," *J. Biomed. Opt.* **10**(2), 024033 (2005).

74. G. Boverman, Q. Fang, S. A. Carp, E. L. Miller, D. H. Brooks, J. Selb, R. H. Moore, D. B. Kopans, and D. A. Boas, "Spatio-temporal imaging of the hemoglobin in the compressed breast with diffuse optical tomography," *Phys. Med. Biol.* **52**(12), 3619–3641 (2007).

75. P. S. Tofts, B. Berkowitz, and M. D. Schnall, "Quantitative analysis of dynamic Gd-DTPA enhancement in breast tumors using a permeability model," *Magn. Reson. Med.* **33**, 564–568 (1995).

76. R. Perini, R. Choe, A. G. Yodh, C. Sehgal, C. Divgi, and M. A. Rosen, "Non-invasive assessment of tumor neovasculature: Techniques and clinical applications," *Cancer Metastasis Rev.* **27**, 615–630 (2008).

77. S. Srinivasan, B. W. Pogue, S. D. Jiang, H. Dehghani, C. Kogel, S. Soho, J. J. Gibson, T. D. Tosteson, S. P. Poplack, and K. D. Paulsen, "Interpreting hemoglobin and water concentration, oxygen saturation, and scattering measured *in vivo* by near-infrared breast tomography," *Proc. Natl. Acad. Sci. U.S.A.* **100**, 12,349–12,354 (2003).

78. L. Spinelli, A. Torricelli, A. Pifferi, P. Taroni, G. M. Danesini, and R. Cubeddu, "Bulk optical properties and tissue components in the female breast from multiwavelength time-resolved optical mammography," *J. Biomed. Opt.* **9**, 1137–1142 (2004).

79. J. Folkman and K. Beckner, "Angiogenesis imaging," *Acad. Radiol.* **7**, 783–785 (2000).

80. B. J. Tromberg, A. Cerussi, N. Shah, M. Compton, A. Durkin, D. Hsiang, J. Butler, and R. Mehta, "Diffuse optics in breast cancer: detecting tumors in pre-menopausal women and monitoring neoadjuvant chemotherapy," *Breast Cancer Research* **7**, 279–285 (2005).

81. H. Dehghani, B. W. Pogue, S. P. Poplack, and K. D. Paulsen, "Multiwavelength three-dimensional near-infrared tomography of the breast: Initial simulation, phantom, and clinical results," *Appl. Opt.* **42**, 135–145 (2003).

82. H. B. Jiang, N. V. Iftimia, Y. Xu, J. A. Eggert, L. L. Fajardo, and K. L. Klove, "Near-infrared optical imaging of the breast with model-based reconstruction," *Acad. Radiol.* **9**, 186–194 (2002).

83. Q. Zhu, N. Chen, and S. H. Kurtzman, "Imaging tumor angiogenesis by use of combined near-infrared diffusive light and ultrasound," *Opt. Lett.* **28**, 337–339 (2003).

84. S. Fantini, S. A. Walker, M. A. Franceschini, M. Kaschke, P. M. Schlag, and K. T. Moesta, "Assessment of the size, position, and optical properties of breast tumors in vivo by noninvasive optical methods," *Appl. Opt.* **37**, 1982–1989 (1998).

85. V. Chernomordik, D. W. Hattery, D. Grosenick, H. Wabnitz, H. Rinneberg, K. T. Moesta, P. M. Schlag, and A. Gandjbakhche, "Quantification of optical properties of a breast tumor using random walk theory," *J. Biomed. Opt.* **7**, 80–87 (2002).

86. E. Heffer, V. Pera, O. Schutz, H. Siebold, and S. Fantini, "Near-infrared imaging of the human breast: Complementing hemoglobin concentration maps with oxygenation images," *J. Biomed. Opt.* **9**, 1152–1160 (2004).

87. S. Srinivasan, B. W. Pogue, C. Carpenter, S. Jiang, W. A. Wells, S. P. Poplack, P. A. Kaufman, and K. D. Paulsen, "Developments in quantitative oxygen-saturation imaging of breast tissue *in vivo* using multispectral near-infrared tomography," *Antioxid. Redox Sig.* **9**, 1143–1156 (2007).

88. T. O. McBride, B. W. Pogue, S. Poplack, S. Soho, W. A. Wells, S. D. Jiang, U. L. Osterberg, and K. D. Paulsen, "Multispectral near-infrared tomography: A case study in compensating for water and lipid content in hemoglobin imaging of the breast," *J. Biomed. Opt.* **7**, 72–79 (2002).

89. R. L. Wahl, "Overview of the current status of PET in breast cancer imaging," *Q. J. Nucl. Med.* **42**, 1–7 (1998).

90. E. Bombardieri and F. Crippa, "PET imaging in breast cancer," *Q. J. Nucl. Med.* **45**(3), 245–55 (2001).

91. S. D. Konecky, R. Choe, A. Corlu, K. Lee, R. Wiener, S. M. Srinivas, J. R. Saffer, R. Freifelder, J. S. Karp, N. Hajjioui, F. Azar, and A. G. Yodh, "Comparison of diffuse optical tomography of human breast with whole-body and breast-only positron emission tomography," *Med. Phys.* **35**, 446–455 (2008).

92. T. Durduran, R. Choe, G. Yu, C. Zhou, J. C. Tchou, B. J. Czerniecki, and A. G. Yodh, "Diffuse optical measurement of blood flow in breast tumors," *Opt. Lett.* **30**, 2915–2917 (2005).

93. C. Zhou, R. Choe, N. Shah, T. Durduran, G. Yu, A. Durkin, D. Hsiang, R. Mehta, J. Butler, A. Cerussi, B. J. Tromberg, and A. G. Yodh, "Diffuse optical monitoring of blood flow and oxygenation in human breast cancer during early stages of neoadjuvant chemotherapy," *J. Biomed. Opt.* **12**, 051903 (2007).

94. P. P. Rosen, *Rosen's Breast Pathology*, Lippincott Williams & Wilkins, Philadelphia (1997).

95. O. E. Silva and S. Zurrida, Eds., *Breast Cancer: A Practical Guide*, Elsevier, Amsterdam (2000).

96. K. Lee, S. D. Konecky, R. Choe, H. Y. Ban, A. Colu, T. Durduran, and A. G. Yodh, "Transmission RF diffuse optical tomography instrument for human breast imaging," in *European Conferences on Biomedical Optics*, OSA, (2007).

97. F. S. Azar, K. Lee, A. Khamene, R. Choe, A. Corlu, S. D. Konecky, F. Sauer, and A. G. Yodh, "Standardized platform for coregistration of non-concurrent diffuse optical and magnetic resonance breast images obtained in different geometries," *J. Biomed. Opt.* **12**, 051902 (2007).

98. B. Davison and J. B. Sykes, *Neutron Transport Theory*, Oxford University Press, London (1957).

99. M. C. Case and P. F. Zweifel, *Linear Transport Theory*, Addison-Wesley, New York (1967).

100. S. F. Ray, *Applied Photographic Optics*, Focal Press, Oxford (2002).

101. R. C. Haskell, L. O. Svaasand, T. Tsay, T. Feng, M. S. McAdams, and B. J. Tromberg, "Boundary conditions for the diffusion equation in radiative transfer," *J. Opt. Soc. Am. A* **11**, 2727–2741 (1994).

102. W. G. Egan and T. W. Hilgeman, *Optical Properties of Inhomogeneous Materials*, Academic, New York (1979).